Back to Session Subjects

Uniformly High Order ENO Schemes for Vortex Convection Across Overset Interfaces

Nathan Hariharan
United Technologies Research Center, East Hartford, CT-06066

Lakshmi Sankar
School of Aerospace Engineering
Georgia Institute of Technology, Atlanta, GA-30332

1.0 Introduction

The flow field around a rotor, whether in forward flight or hover, is difficult to model due to the presence of strong vorticity. The flow phenomena for a rotor differ from that for a wing-in-forward-flight, because of the differing influence of their respective wakes. For a wing in forward flight, the generated tip vortex and the vortex sheet are quickly convected away from the wing, and the influence of the shed wake on the flow field in the vicinity of the wing is small. For an adequate numerical simulation of a wing in forward flight, it is sufficient to capture the generated tip vortex in the vicinity of the wing. In contrast, in the flow field around a rotor, the strong vortex wake system lingers in the vicinity of the rotor. In hover, the strong tip vortex coils beneath the rotor, and significantly alters the effective angle of attack of the rotor.

Accurate numerical prediction of aerodynamic parameters such as thrust coefficient and induced torque coefficient requires an accurate modeling of the tip vortex. In forward flight the entire vortex system is swept back leading to strong interaction between blade-tip vortices with successive blades, a phenomenon known as the blade-vortex interaction (BVI). These blade vortex interactions result in rapid changes in local flow conditions and are a major source of aerodynamic noise and structural vibration.

The underlying issue in modeling these flows is the necessity to fully account for the complex vortex system generated by the rotor. Researchers in the past two decades have adopted a broad class of methodologies with various levels of complexity to model the vortex system. Until recently this representation was externally input from empirical/analytical models because full Euler/Navier-Stokes (NS) computations were infeasible. With the enormous advances in computational methodologies and computational power researchers have been adapting Euler/NS techniques for the study of the rotor-flowfield. These solvers are particularly useful in analyzing new or complex rotor blades where no experimental data is available. Studies by Srinivasan and Ahmad[1], Strawn and Barth[2], and Duque[3, 4] have used a variety of strategies such as unstructured methodologies, and overset methodologies to tackle this problem. An excellent survey article by McCroskey[5] gives a comprehensive review of modern computational strategies for rotor applications.

Such methodologies that solve for the flow field from the basic conservation laws without using additional information (information from analyses such as other numerical

formulations, analytical formulations, or experimental observations) are generally referred to as "first-principles" based methods. Traditional low-order spatially accurate Euler/Navier-Stokes computational methodologies tend to dissipate the vortex wake system due to the high numerical dissipation inbuilt in such numerical schemes[5]. Some amount of dissipation is essential for numerical schemes to damp high frequency oscillations. However, such a procedure should not diffuse legitimate flow features –such as vorticity- that exhibit sharp gradients in flow properties.

One of the earliest, relatively successful, attempt to build a high fidelity, low numerical dissipation, high order scheme adopted Essentially Non-Oscillatory (ENO)[6-8] methodologies in order to capture 3-D rotary-wing vortex wakes. In recent years various other approaches to building high order schemes for rotor wake capturing have also been proposed. Schemes such as DRP schemes[9] and projected MUSCL[10] have been tried out for studying rotorcraft wakes with varying degrees of success. Compact high order schemes – schemes that use information only from any given cell and its neighbors – such as Discontinuous Galerkin[11] have been only moderately successful for 3D unsteady vortex capturing so far. More research is needed to refine high order methods further to arrive at an optimal scheme applicable for 3D calculations.

This paper focuses upon the use of fifth/seventh order spatially accurate, Essentially Non-Oscillatory schemes for capturing vortices while minimizing numerical dissipation. One of the drawbacks with ENO schemes is that they are not compact, and hence a wide stencil of information is required to construct the high fidelity solution. This becomes a problem when large scale simulations are broken into parts and distributed over a computing network, making it necessary to have sufficient overlap between the grid-parts to construct uniformly high order accurate solution. One possible solution is to let the adaptive underlying methodology of ENO to construct one-sided high order solutions near the grid boundaries created due to a distributed grid-partition. This work explores three different implementations of the numerical treatment of 7^{th} order ENO schemes near overset grid boundaries. The relative merits of these schemes for capturing vortex wakes arising from wings and rotor-blades are summarized.

2.0 High-Order Methods for Accurate Prediction of the Wake

The discretized form of the 3D, unsteady finite-volume version of the Navier-Stokes equation was solved:

$$\frac{\partial}{\partial t}\left(q\Omega_J\right) + \sum_{i=1}^{6}\left(\left(\vec{V}_F - \vec{V}_G\right)q + F\right)\cdot \Delta S = \sum_{i=1}^{6} F_v \cdot \Delta S \tag{1}$$

The above formulation allows for arbitrary motion of the grids. The temporal discretization is implemented using a three-point stencil, and the solution update process uses a Newton iterative solver to achieve third order temporal accuracy. The viscous fluxes are computed using central differences. The inviscid fluxes are updated using an approximate Riemann solver, i.e., the numerical flux on the cell faces is given by,

$$F = \frac{F_1(q_L) + F_1(q_R)}{2} - |A|(q_R - q_L) \tag{2}$$

2.1 Fifth/Seventh Order Essentially Non-Oscillatory (ENO) Scheme

The fifth/seventh high order formulation for Navier-Stokes Solution has been developed along the lines of Essentially Non-Oscillatory (ENO) methods developed originally by Harten[12]. The higher order reconstruction comes in the projection stage of the conservative variable, i.e., q_L and q_R. For a smoothly varying function, these projections are based on the support stencils shown in the Figure 1a.

The details of the implementation are provided elsewhere[7, 8]. The formulation is briefly discussed below for completeness. The high order reconstruction for a 3-D flowfield solution is broken down as three independent 1-D reconstructions in the three computational dimensions. Such a breakdown keeps the overall computing efforts within a manageable limit while retaining a large portion of the benefits of the high order reconstruction. The high order ENO reconstruction in a single dimension is described below.

For a one dimensional initial boundary value problem, the system of hyperbolic conservation laws may be written as,

$$q_t + \nabla f(q) = 0\,,\ q(x,0) = q_0(x), \tag{3}$$

The updated solution at the next time step, n+1, can be written as,

$$q_j^{n+1} = A(C_j)E(\tau)R\left(x; q^n\right) \tag{4}$$

Here, q's are the cell averaged state variables, R is the reconstruction polynomial approximation of the actual solution over the cell, constructed using the available cell averages, E is the evolution operator that advances the solution by a given time step, and A is the averaging operator over cell C_j to get back the cell averages at the next time step. The high order reconstruction can either be directly applied to the fluxes themselves, or to the cell averaged state variables prior to using those values to compute the fluxes. In this work, the second approach was used. The high order construction was applied to the state variables and the approximate Riemann solver used as the evolution operator. The fifth order reconstruction is done as follows.

Let J(i) be the vector containing the stencil index for the i-th grid point, and C_j denote the cell associated with node-j. Given the cell averages q_j of a function q'(x) we need reconstruction R such that,

$$R(x;q) = q'(x) + O\left(h^r\right),\ \ A(C_j)R(x;q) = q_j\ ,\ \ j \in J(i) \tag{5}$$

where r is the required order of accuracy. The polynomial R can be expressed as a Taylor expansion around the centroid of cell i.

$$R_i(x;q) = \sum_{k=0}^{i=1} \frac{1}{k!}(x - c_i)^k D_k\,,\ \ D_k = \frac{\partial^k q'}{\partial x^k}(c_i) + O\left(h^{r-k}\right) \tag{6}$$

The D_k's may be evaluated by,

$$A(C_j)R_j = q_j, \quad j \in J(i) \tag{7}$$

This yields a system of equations for the D_k's,

$$\sum_{k=o}^{i=1} a_{j,k} D_k = q_j, \; j \in J(i)$$

$$a_{j,k} = \frac{1}{k!} A(C_j)(x - c_i)^k = \frac{1}{k!|C_j|} \int_{C_j} (x - c_i)^k dV, \; |C_j| = \int_{C_j} dV \tag{8}$$

Inverting the above system, the D_k's are determined. Using these values of D_k's, R can be constructed using Equation (6).

An economic stencil adapting strategy is adopted in the implementation. For a fifth order scheme there are five possible stencil variations that will include cell 'i', for either q_L or q_R. For a smooth flow the most symmetric stencil (with an upwind directional bias of half a cell) is preferred. In the present implementation the stencil to be used for each point is stored. In case of a smooth flow, the stencil pattern is set once after the flow solver is initiated. In case of unsteady flow with shocks, the stencil adaptation is done throughout all the domains at every so many time steps (typically every 10 time steps). At every grid point, the stencil to be used is decided by comparing a weighted absolute value of the derivatives, as shown below.

$$D_{sum} = \sum_{k=0}^{i=1} \alpha_k |D_k| \tag{9}$$

The derivatives are weighted by factors α_k. The weighting factors are set to give a hierarchical preference to the most centered stencil (most preferred), followed by slightly one-sided stencil and finally to the most one-sided stencil (least preferred), in the regions where flow properties are smooth. Such a preference will rule out wild oscillations of the stencil due to minor changes in the derivatives at every time step. This will ensure that unless discontinuities are encountered in the flowfield the centered stencil is preferred. In case a discontinuity is present in the sampling region, i.e., as illustrated in Figure 1b, the sampling stencils are automatically shifted to avoid sampling across the discontinuity, as shown in Figure 1c.

The time stepping is done in an implicit manner using directional factorization[13]. A third order Newton iterative scheme is used to integrate in time. The temporal update was done using a three point temporal stencil, i.e.,

$$\frac{\partial}{\partial t}\left(q^{n+1}\right) \cong \frac{\left(3q^{n+1} - 4q^n + q^{n-1}\right)}{2\Delta\tau} + O\left(\Delta\tau^2\right) \tag{10}$$

The seventh order ENO scheme is constructed along similar lines as above. A wider stencil as shown in Figure 2 is used for the left and right projection. The stencil shifting near the boundaries and discontinuities is similar to the fifth order implementation.

3. Advanced Methods for Convection of Vortex Across an Overset Interface

ENO, and weighted-ENO (WENO) schemes utilize large stencil support for constructing progressively high order accuracy spatial schemes. The handling of such schemes near overset boundaries influences the overall solution accuracy for large-scale computations. An ENO

based $5^{th}/7^{th}$ order spatially accurate Euler/Navier-Stokes overset solver was utilized to study the convection of vortices across overset interfaces. Different treatments of fifth/seventh schemes near overset interfaces was studied in some detail using different overset-grid configurations. In section 3.1 three different implementations are discussed, and their ability to preserve a vortex convecting across is studied for using a pair of grids with the minimal possible overset interface. In section 3.2 the minimal overlap condition for the oversetting is relaxed, and also the effect of multiple interpolation layer is discussed. In section 3.3 the convection across overset grids with varying grid densities is explored.

3.1 Minimal Overlap of Grids

Three different numerical formulations near the boundary interfaces were constructed, and their ability to preserve high order solution accuracy near the overset interface boundaries was studied. Two overlapping Cartesian meshes were generated, and a Lamb's vortex was convected across the overset interface between the two meshes. The mesh is shown in figure 3. The grids constructed were 3D. Symmetric boundary conditions were enforced in the y-direction. The Lamb's vortex that was introduced with its axis aligned in the y-direction. In principle, excessive oversetting causes computational in-efficiency, i.e., the same physical domain is computed by two different set of grid points, and one would like to minimize such overlaps. This is especially true for large-scale rotor flow computations wherein oversetting is used as a means of grid break-up, or refinement for parallel computations. From the standpoint of preservation of a vortex transferring across overset interfaces, the minimal interface poses the most stringent requirements for non-comapct high order schemes as such schemes require a wide-stencil support.

Three different implementations of the fluxes near the overset boundaries for Grid-1(G1), and Grid-2(G2) were considered. Figure 4 shows a 1-D schematic of the first implementation (Method-1). In this case, the boundary points of G1 were interpolated from G2, and vice-versa. The computation order of accuracy near the boundary cell were dropped to first order, i.e.,

$$q^{G1}_{NMAX} = q^{G2}_{3}$$
$$q^{G2}_{1} = q^{G1}_{NMAX-2}$$
$$q^{G1}_{R,NMAX-1} = q^{G1}_{NMAX}$$
$$q^{G1}_{L,NMAX-1} = q^{G1}_{NMAX-1}$$
$$q^{G2}_{R,1} = q^{G2}_{2}$$
$$q^{G2}_{L,1} = q^{G2}_{1}$$

(11)

The Lamb's vortex was initiated in the center of G1. Figure 5 (a-j) shows a sequence of images showing the vortex as it convects down, and across the overset interface. The vortex is well within G1 in figures 5a, and 5b, and is seen to be in full strength without any distortions. As it approaches the interface (figure 5c), the vortex starts to distort. The vortex begins to transfer to G2 in figure 5d, and is clearly seen to appear in G2 in a dissipated form. The contour plots in the overlap region consist of the vorticity in G1, and G2 as well. If the vortex is transferred perfectly, the contours should be identical. Figures 5e-h capture the process of the vortex crossing over the interface. The vortex has completely transferred over to G2 in figures 5i,j. The use of Method-1 boundary treatment results in a significant loss of resolution of the vortex during the transfer process.

Figure 6 shows the plots of tangential velocity variation across the vortex at several instances in the process of the vortex crossover. A single crossover results in the peak-to-peak strength of the vortex to be reduced by approximately 40%. The use of Method-1 would largely negate any advantages of the current high order scheme if multiple overset grids were used.

In order to improve the accuracy near the interface, Method-2 was developed. Figure 7 shows a schematic illustrating Method-2. In Method-2, the adaptive nature of the stencils in a ENO-scheme is used to construct 7^{th} order accurate solution all the way to the overset interface. This is achieved by shifting to one-sided stencils near the boundaries. In figure 7, the two stencils employed to compute q_L, and q_R for faces (NMAX-1, G1), and (1, G2) are shown. The left, and right stencils are staggered by one cell difference. The treatment of the fluxes near the overset interface can be summarized as,

(12a)

$$q^{G1}_{NMAX} = q^{G2}_{3}$$
$$q^{G2}_{1} = q^{G1}_{NMAX-2}$$
$$q^{G1}_{R,NMAX-1} = ENO(q^{G1}_{R,NMAX-1})$$
$$q^{G1}_{L,NMAX-1} = ENO(q^{G1}_{L,NMAX-1})$$
$$q^{G2}_{R,1} = ENO(q^{G2}_{R,1})$$
$$q^{G2}_{L,1} = ENO(q^{G2}_{L,1})$$

for the grid points (NMAX, G1), and (1,G2), and

(12b)

for the primitive variables at the cell faces (NMAX-1, G1), and (1, G2). In equation (12b), the ENO(.) operator stands for the projection using the 7th order ENO method.

Figure 8(a-j) shows a sequence of images for computations using Method-2, similar to figure 5, showing a vortex as it convects down, and across the overset interface. The vortex is well within G1 in figures 8a, and 8b, and is seen to be in full strength without any distortions. As it approaches the interface (figure 8c), the vortex doesn't distort. The vortex begins to transfer to G2 in figure 8d, and as can be seen in images 8d-f, the vortex transfers in an intact form without excessive dissipation. The vortex has completely transferred over to G2 in figures 8i,j, at which point it has dissipated to some extent when compared to the original vortex in G1.

Figure 9 shows the plots of tangential velocity variation across the vortex at several instances in the process of the vortex crossover, for Method-2. A single crossover results in the peak-to-peak strength of the vortex to be reduced by approximately 10%. The use of Method-2 would still result in significant loss of vortex strength if several overset grids were used in a computation. For accurately capturing Blade-Vortex interaction noise phenomena, the tip vortex from a rotor-blade has to be captured without dissipation for over 3-4 blade revolutions. A typical distributed, overset grid computation would involve several overset interface information transfer before the tip vortex travels such distances.

Method-3 was developed to further improve the accuracy of the computation near the interfaces, and it leverages ENO projection of face fluxes. Figure 10 shows a schematic illustrating Method-2. First, as in Method-2, one-sided stencils are used near the interface boundaries. Further, the primitive variables at the two cell faces near the interface boundary (NMAX-1,G1), and (1,G2) are directly interpolated from each other. The interface treatment can be summarized as,

(13a)

$$q^{G1}_{NMAX} = q^{G2}_{3}$$
$$q^{G2}_{1} = q^{G1}_{NMAX-2}$$

for the grid points (NMAX, G1), and (1,G2), and

$$q^{G1}_{R,NMAX-1} = ENO(q^{G2}_{R,2})$$
$$q^{G1}_{L,NMAX-1} = ENO(q^{G2}_{L,2})$$
$$q^{G2}_{R,1} = ENO(q^{G1}_{R,NMAX-2})$$
$$q^{G2}_{L,1} = ENO(q^{G1}_{L,NMAX-2})$$

(13b)

for the primitive variables at the cell faces (NMAX-1, G1), and (1, G2).
Figure 11(a-j) shows a sequence of images for computations using Method-2, similar to figures 5, and 8. The vortex contours in G1, and G2 appear almost identical as the vortex overlays the interface. The vortex appears in G2 (figure 8j) intact with no noticeable

dissipation. Figure 12 shows the plots of tangential velocity variation across the vortex at several instances in the process of the vortex crossover, for Method-3. A single crossover results in the peak-to-peak strength of the vortex to be retained. The use of Method-3 would be desirable to retain all advantages of high order scheme if several overset grids were used in a computation. Figure 13 compares all the vortex strength as computed by the three methods in a single plot.

3.2 Excess Overlap of Grids

In the above section different treatments of higher order boundaries were considered for the minimal-overlap concept. Minimal overlap is desirable from the standpoint of computational efficiency, and becomes vital if a large grid is distributed among a number of processors. For example, a background Cartesian grid to compute rotor in hover, consisting of 25 million grid points, may be broken up into 25 distributed pieces. In such a case, having excessive overlap in all three directions will result in a substantial number of grid points covering the same region of space.

However, there may be other instances where the two-cell overlap may be excessively restrictive. For example, when a C-type grid is placed in a background grid the "fringe" point overset boundaries of the background grid are usually set at least 5-6 points within the C-grid far-field boundaries. Such overset boundary points associated with body grids do not repeat a large number of times as in a distributed break-up, and hence one can tolerate some computational inefficiency.

In this section we investigate the three methods outlined in section 3-1 when the minimal overlap condition is relaxed. Figure 14 shows the Cartesian grid system showing the two grids with the overlap region consisting of 25 grid cells. In this study, the initial core size of the vortex was varied from 4 to 10 cells across the peak-to-peak variation. Therefore, even for the well resolved case of 10 cells across the vortex core, the vortex will always be well within either one of the grids at all times as it convects across. The variation in core-size was done to arrive at the minimal grid requirement metrics in the Cartesian settings.

Figure 15 shows a carpet plot of the tangential velocity variation, for the 7^{th} order ENO solution, across the vortex at various streamwise locations as the vortex moves across. The boundary treatment outlined in Method-1 was applied at the interfaces. The plots span Grid-1 (black), and Grid-2 (dashed red). The grid point locations are also identified for the Grid-1 plots in order to ascertain the number of grid points between the peak-to-peak tangential velocity variation. The vortex was initialized in Grid-1, as before, but with 4 grid points across the vortex core. Two issues are of interest. The first is the diffusion not related to boundary treatment effects. Even within Grid-1, the peak-to-peak variation decays as the 7^{th} order scheme cannot hold the initial prescribed vortex at 4 points across the core without diffusion. The number of grid points across the core tends to settle down at 5-6 points across the core, as seen from the downstream stations. The second issue is the decay at the inter-grid boundary if Method-1 is applied. As one would expect, guided by results in the earlier section, there is more than 30% decay of the peak-to-peak core velocity as the vortex transfers to Grid-2. This result was similar to the minimal overlap case using Method-1 discussed in the last section. Using first order boundary treatment will be equally detrimental irrespective of minimal or excessive grid overlap.

Figure 16 shows a similar plot using Method-2. The initial core size was still maintained at 4 grid points across, and hence the overall peak-to-peak decay to 5-6 grid points was similar. However, at the interface the peak-to-peak variation was captured in Grid-2 with no noticeable dissipation, but with a small shift in the vortex location. Compared to the minimal overlap case, the vortex is transferred across to Grid-2 with higher fidelity. This is to be expected as only one grid uses one-sided stencils near the boundary interface when there is excess grid overlap. The shift in the vortex location was less than 5% of the vortex core size. Such a shift may affect computations which require an accurate vortex position, i.e., rotor-blade in hover wherein the location of the first-passage vortex plays a large part in accurately determining the tip loads.

Figure 17 shows a similar plot when Method-3 is used. At the interface the vortex is transferred to Grid-2 with no noticeable difference in the core structure. Irrespective of whether the oversetting is minimal or excessive, Method-3 produces the cleanest transfer. However, for the excess overlap case Method-2 introduces only small discrepancies in the transferred vortex strength, and location. Figure 18 shows the result when 5^{th} order scheme is used instead of 7^{th}. The overall dissipation associated with 5^{th} order is higher (vortex will settle down eventually at ~10 points across core), but the interface transfer characteristics are similar to the 7^{th} order result in figure 17.

In the excess overlap settings, an alternative to directly interpolating the fluxes as in Method-3 is to interpolate multiple layers of internal boundary points. Figure 19b illustrates this concept for two layers of interface interpolation (usually referred in the overset literature as “double layer”). The first two streamwise layers of Grid-2, and the last two streamwise layers of Grid-1 derive their flow information from each other respectively. Figure 19a shows the standard single-layer concept for comparison. For obvious reasons, one cannot implement double-layer interpolation when the overlap region is two or three cells.

Since from the earlier studies in this section it was established that the 7^{th} order scheme required 5-6 grid points across the core to avoid dissipation, the vortex was re-initialized with 6 grid points across the core. Figure 20 shows the familiar carpet plot of the tangential velocity variation at several location across the vortex path. For this study of single vs. double interpolation layer only Method-2 was used at the interface. For the single interpolation study, the vortex is transferred across with no noticeable dissipation, but with a small shift in vortex position. Figure 21 shows similar results for double-layer interpolation. In this case the vortex computed on the two grids lie right on top of each other. Using three layers of interpolation does not offer any further benefits, as seen in figure 22. This study shows that, wherein excess overlap is possible, Method-2 with double-layer interpolation is sufficient.

3.3 Overset Grids with Resolution Mismatch

So far in we have only considered vortex transfer between grids that are identical in resolution. Often in practice enforcing such a criteria may not be possible, and there may be some mismatch. In this section we look at some bounds on how much the resolution can be different without introducing any significant distortion in strength, and position of the transferred vortex.

Figure 23 shows the grid system for this study. Grid-1 has twice as much resolution as Grid-2, and is immersed entirely inside Grid-2. The vortex was initialized inside Grid-1. The transfer to Grid-2 occurred through internal boundary points generated by cutting a hole in Grid-2.

Such points are generally referred to as “fringe” points. Figure 24a shows a sequence of vorticity contour plots in Grid-1 as the initialized vortex transports across to the streamwise-end of Grid-1. Figure 24b shows similar vorticity contour plots in Grid-2, as the vortex transfers across from Grid-1 through the fringe points, and transports across Grid-2. Periodic boundary conditions had been implemented at the streamwise boundaries for Grid-2, and hence the vortex feeds back into the upstream location (as seen in figure 24b).

The vortex was first initialized in Grid-1 to be well-resolved for the 7^{th} order scheme, i.e., 9 grid points across the vortex core. For this study Method-2 was used at the inter-grid boundary interfaces. Figure 25 shows the comparison of tangential velocity variation across the vortex at a location identified as Station-A in figure 24a. Station-A is a streamwise location inside the common overlap region of Grid-1, and Grid-2, i.e., between the fringe boundary of Grid-2, and downstream boundary of Grid-1. As can be seen in figure 25, the transferred vortex in Grid-2 has no noticeable loss in strength. This can be explained if one looks at the relative grid resolutions of the two grids in comparison with what is required by the 7^{th} order scheme to preserve the vortex without any loss. The 7^{th} order scheme requires 5-6 grid points across the vortex core to transport without any noticeable loss in vortex strength. In this case the vortex was initialized at 9 grid points on Grid-1, which is more than necessary for the 7^{th} order scheme. Grid-2 is half the resolution as Grid-1, and would have a resolution of 5 grid points ((9+1)/2) across the core. For the 7^{th} order scheme, this is just sufficient, and hence there is no noticeable loss in peak-to-peak strength in the transferred vortex.

Next, the vortex was re-initialized with 7 grid points across the core in Grid-1, and the above study was repeated. Figure 26 shows a similar comparison of the vortex strengths at Station-A. In this case, the Grid-2 has a resolution of 4 grid points across the core, which is less than what is required by the 7^{th} order scheme. One would expect some degradation of the transferred vortex, which indeed is the case. The peak-to-peak strength of the vortex in Grid-2 is about 85% the strength in Grid-1 at Station-A. This study was further repeated with 5 grid points (just resolved) across the vortex core in Grid-1, which puts it at 3 grid points (under-resolved) across the core in Grid-2. Figure 27 shows the similar comparison of the vortex strengths in Grid-1, and Grid-2, the transferred vortex can be seen to be captured at ~50% peak-to-peak strength of the original vortex. Thus, if the grids are mismatched, as long as both the grids satisfy the minimum grid point requirements for the scheme being used, no noticeable degradation occurs in the transferred vortex. It must be noted that for the Lamb’s vortex that was considered in this study the dominant gradient exist only along the tangential direction. However, for realistic 3D vortices coming off a wing, or a rotor, often a strong axial velocity component exists within the vortical structures. For such vortices, the grid resolution requirements should ensure that the axial gradients, which are stronger than the tangential gradients, are captured. If that is not the case, the axial velocity components will be diffused out, and the vortex itself will diffuse in order to maintain angular momentum conservation. This effect is illustrated in a numerical study of tip vortex evolution off a NACA0015 wing by Hariharan[16].

4.0 Conclusions

In this paper the advantages of careful treatment of overset boundaries for ENO based high order methods in capturing vorticity were outlined. One of the drawbacks with ENO schemes is that they are not compact, and hence a wide stencil of information is required to construct the high fidelity solution. This becomes a problem when large scale simulations are broken into parts and distributed over a computing network, making it necessary to have sufficient

overlap between the grid-parts to construct uniformly high order accurate solution. One possible solution is to let the adaptive underlying methodology of ENO to construct one-sided high order solutions near the grid boundaries created due to a distributed grid-partition. A seventh order near boundary ENO scheme treatment, using such one-sided stencils, and direct primitive variables interpolation, has been demonstrated to capture vortices convecting across overset interfaces with no noticeable dissipation, in Cartesian grid settings. This scheme is a likely candidate for computing rotor-blade wakes using Cartesian background grids, for application such as Blade-vortex interaction noise. Further research is needed to generalize such ENO high order interface methods for non-Cartesian grids.

References

[1]Srinivasan, G.R., and Ahmad, J.U., "Navier-Stokes Simulation of Rotor-Body Flowfield in Hover Using Overset Grids," Paper No. C15, CEAS 19th European Rotorcraft Forum, Cernobbio, Italy, September 1993.

[2]Strawn, R.C., and Barth, T. J., "Unstructured Adaptive Mesh Computations of Rotorcraft High-Speed Impulsive Noise," *Journal of Aircraft*, Vol. 32, No. 4., 1996.

[3]Duque, E.P.N., and Srinivasan, G.R., "Numerical Simulation of a Hovering Rotor using Embedded Grids," 48th Annual AHS Forum, Washington D.C., May 1992.

[4]Duque, E.P., "A Structured/Unstructured Embedded Grid solver for Helicopter Rotor Flows," 50th Annual AHS Forum, Washington D.C., May 1994.

[5]McCroskey, W.J., "Wake Vortex System of Helicopters," AIAA-95-0530, Reno, NV, January 1995.

[6]Harten, A., Engquist, B., Osher, S., and Chakravarthy, C.R., "Uniformly High Order Accurate Essentially Non-oscillatory Schemes III," *Journal of Computational Physics*, Vol. 131, No. 1, pp. 3-47, February 1997.

[7]Hariharan, N., and Sankar, L.N., "Higher Order Numerical Simulation of Rotor Flow Field, AHS Forum and Technology Display," Washington, D.C., May 1994.

[8]Hariharan, N., Sankar, L.N., "Application of ENO Schemes to Rotary Wing Problems," AIAA-95-1892, 13th AIAA Applied Aerodynamics Conference, San Diego, CA, June 1995.

[9]Hall, C.M. and Long, L.N., "High-Order Accurate Simulations of Wake and Tip Vortex Flowfields," AHS 55th Annual Forum, Montreal, Canada, May 1999.

[10]Tang, L. and Baeder, J.D., "Improved Euler Simulation of Hovering Rotor Tip Vortices with Validation," AHS 55th Annual Forum, Montreal, Canada, May 1999.

[11]Hariharan, N., "A First-Principles Based High Order Discontinuous Galerkin (DG) Methodology for Rotorcraft Flowfield Studies," NASA SBIR Phase-I Report NAS2-98062, CFD Research Corporation, Huntsville, AL, October 1998.

[12]Harten, A., Engquist, B., Osher, S., and Chakravarthy, C.R., "Uniformly High Order Accurate Essentially Non-oscillatory Schemes III," *Journal of Computational Physics*, Vol. 131, No. 1, pp. 3-47, February 1997.

[13]Hariharan, N. and Sankar, L.N., "Numerical Simulation of Rotor-Airframe Interaction," 33rd AIAA Aerospace Sciences Meeting, Reno, NV, January 1995.

[14]Caradonna, F.X. and Tung, C. "Experimental and Analytical Studies of a Model Helicopter Rotor in Hover ", Vertica, Vol 5, pp149 to 161, 1981.

[15]Srinivasan, G.R and Baeder, J.D., "TURNS: A Free Wake Euler/Navier-Stokes Numerical Method for Helicopter Rotors," AIAA Journal, Volume 31, Number 5 May 1993.

[16]Hariharan, N., "Rotary-Wing Wake Capturing: High Order Schemes Towards Minimizing Numerical Vortex Dissipation," Journal of Aircraft, Volume 39, No.5, September-October 2002, pp 822-830.

.

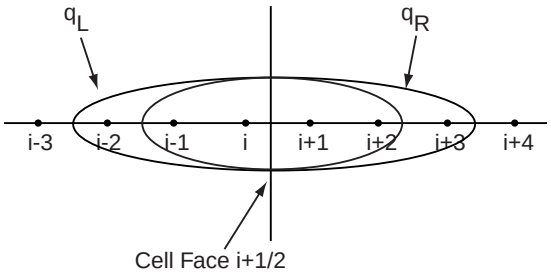

Figure 1a. Fifth Order Stencils for Computing Left and Right Primitive Variables.

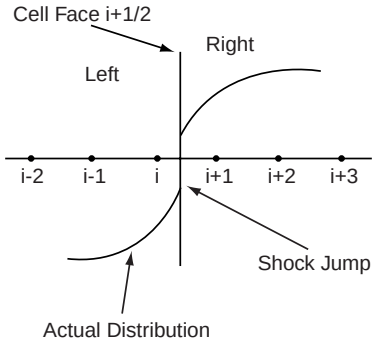

Figure 1b. Illustration of a Distribution with a Discontinuity.

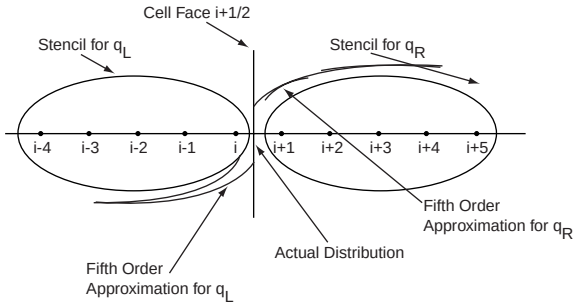

Figure 1c. Adaptive Stencil for Uniformly High Order Solution.

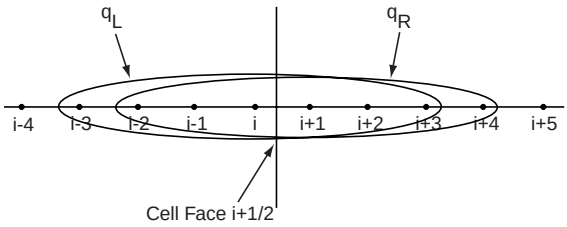

Figure 2. Seventh Order Stencil for Smooth Flow Conditions.

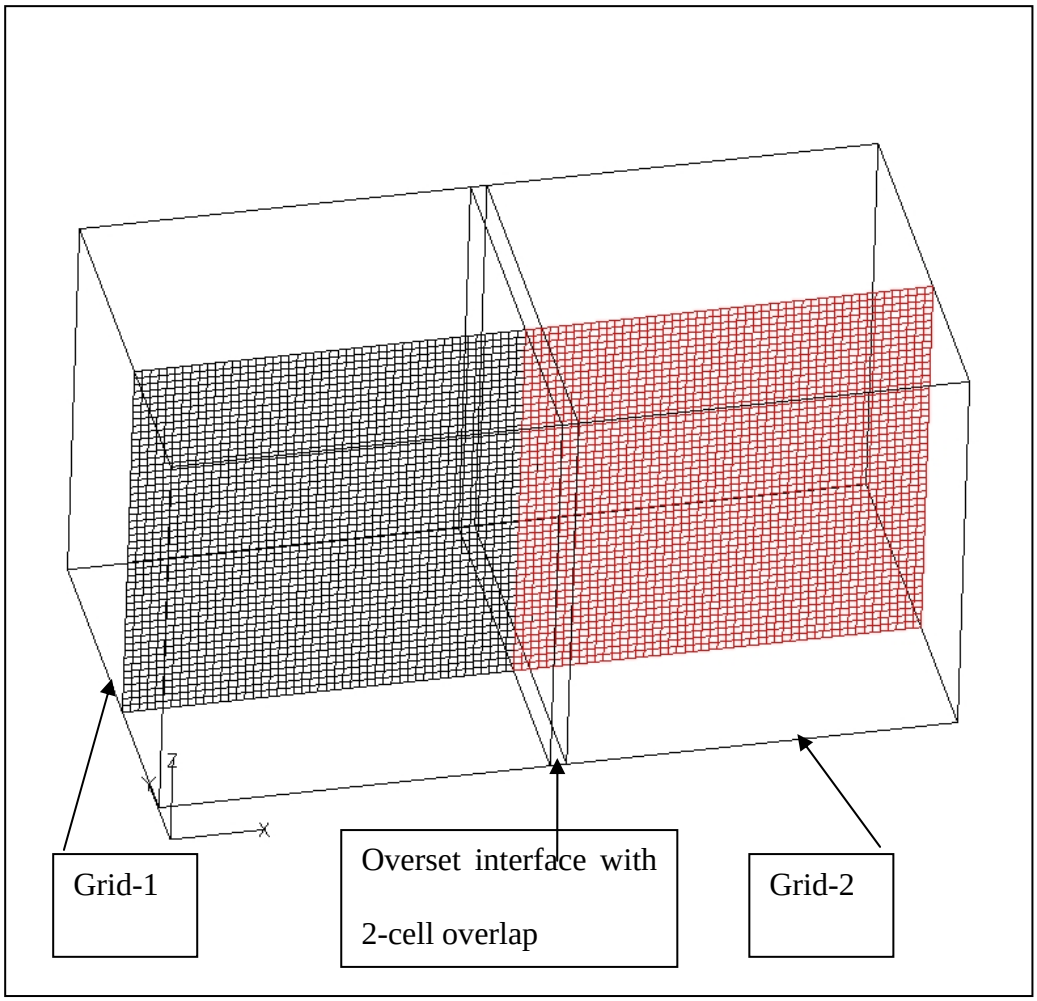

Figure 3. Overset grids with two-cell overlap.

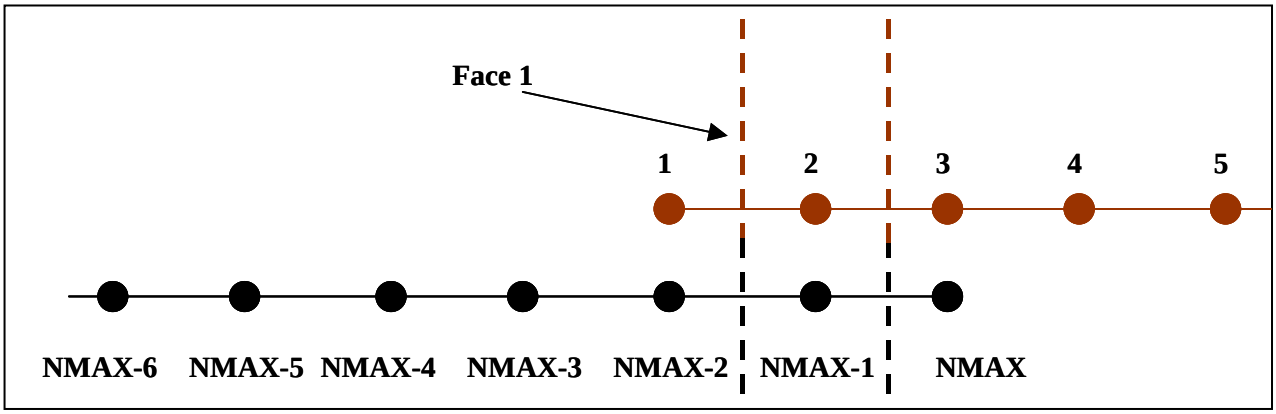

Figure 4. Schematic of the treatment of the fluxes near the overset interface. Method-1: First-order near the overset interface.

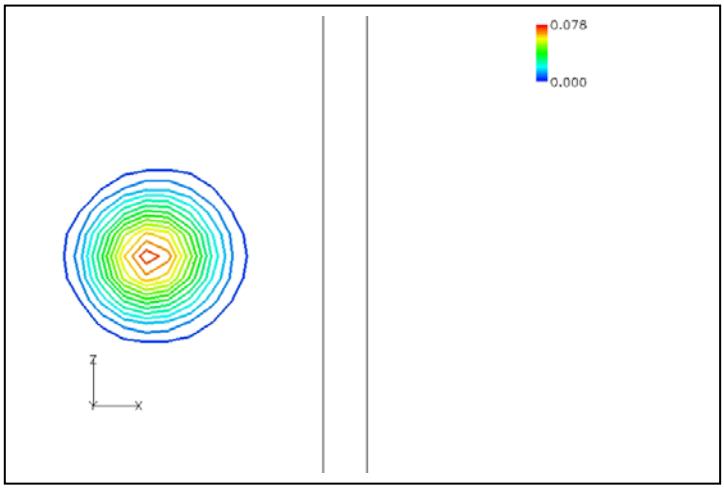

a

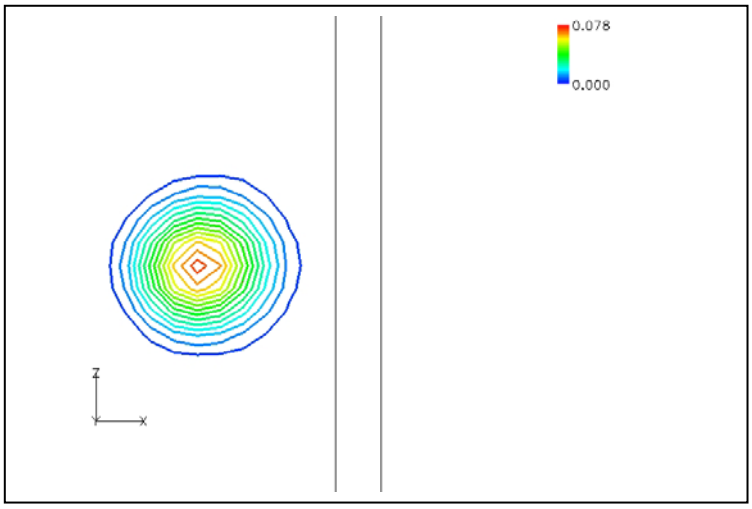

b

Figure 5. Vorticity contours showing Lamb's vortex propagation across interface. Method-1: First-order near the overset interface.

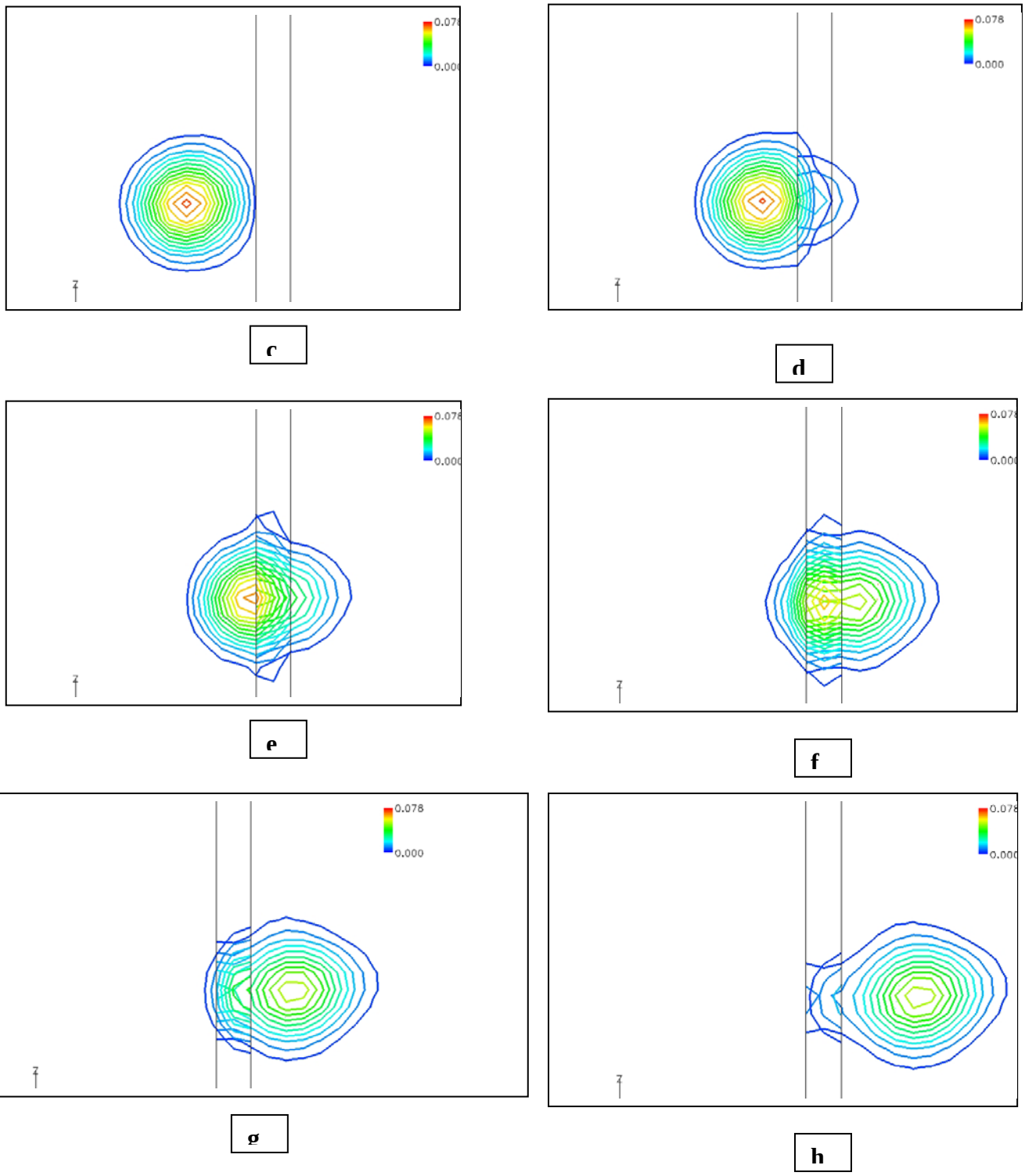

Figure 5 (continued). Vorticity contours showing Lamb's vortex propagation across interface. Method-1: First-order near the overset interface.

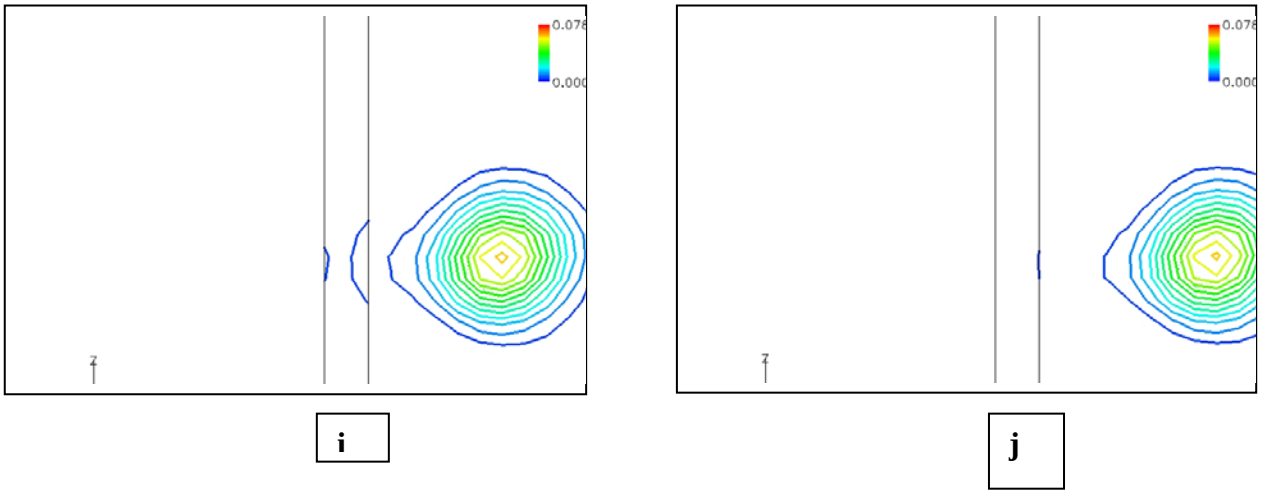

Figure 5 (continued). Vorticity contours showing Lamb's vortex propagation across interface. Method-1: First-order near the overset interface.

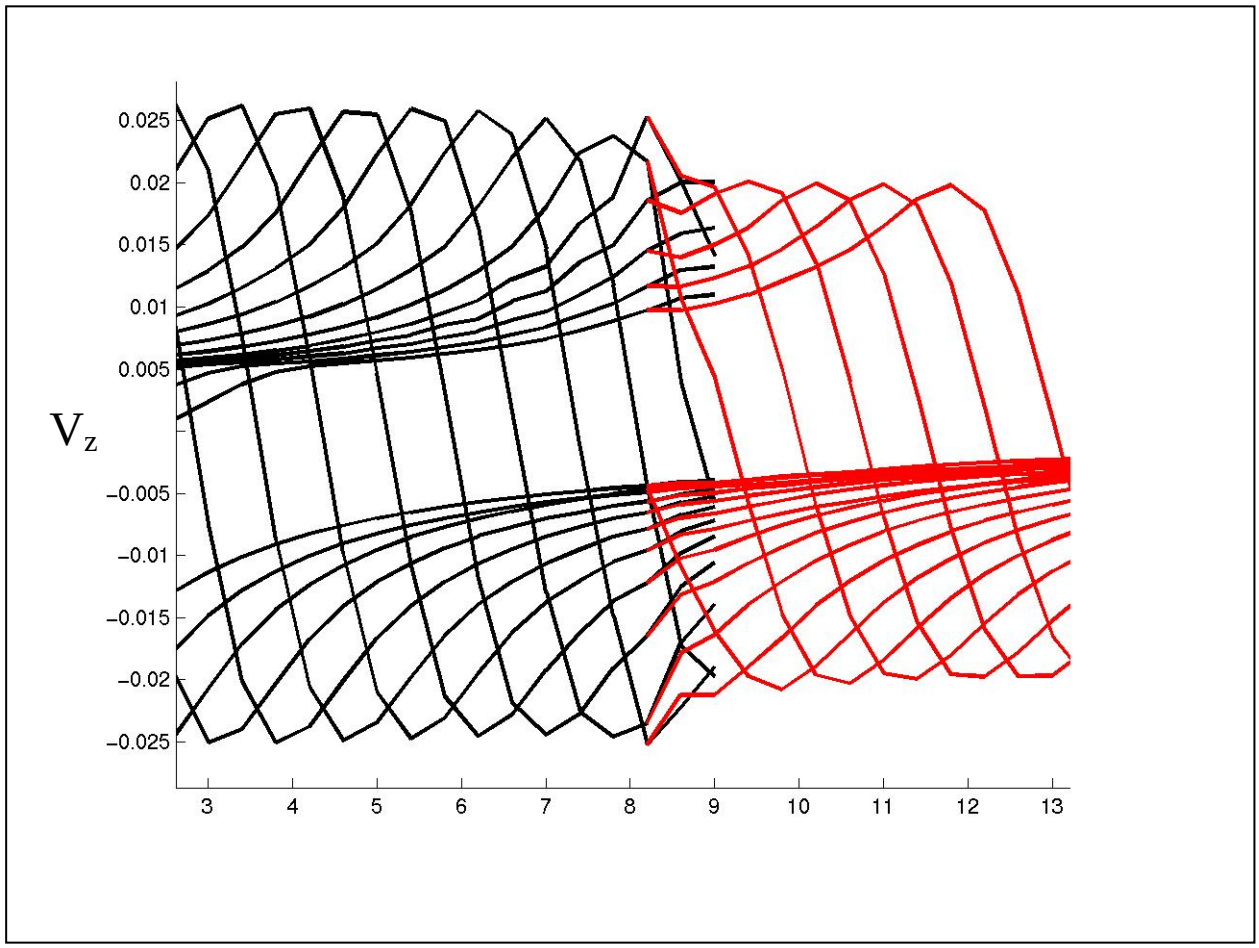

Figure 6. Tangential velocity distribution across the vortex, as it convects through the interface (Black is on Grid-1, Red is on Grid-2). Method-1: First-order near the overset interface.

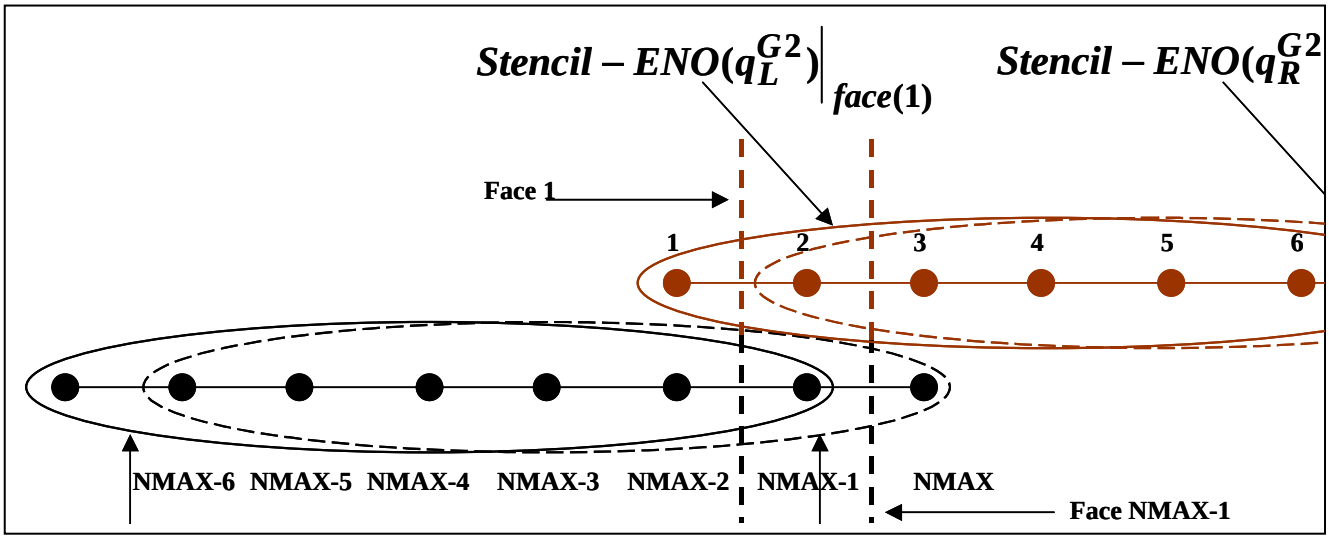

Figure 7. Schematic of the treatment of the fluxes near the overset interface. Method-2: Uniformly 7th order ENO computation over the entire domain, using one-sided stencils near boundaries.

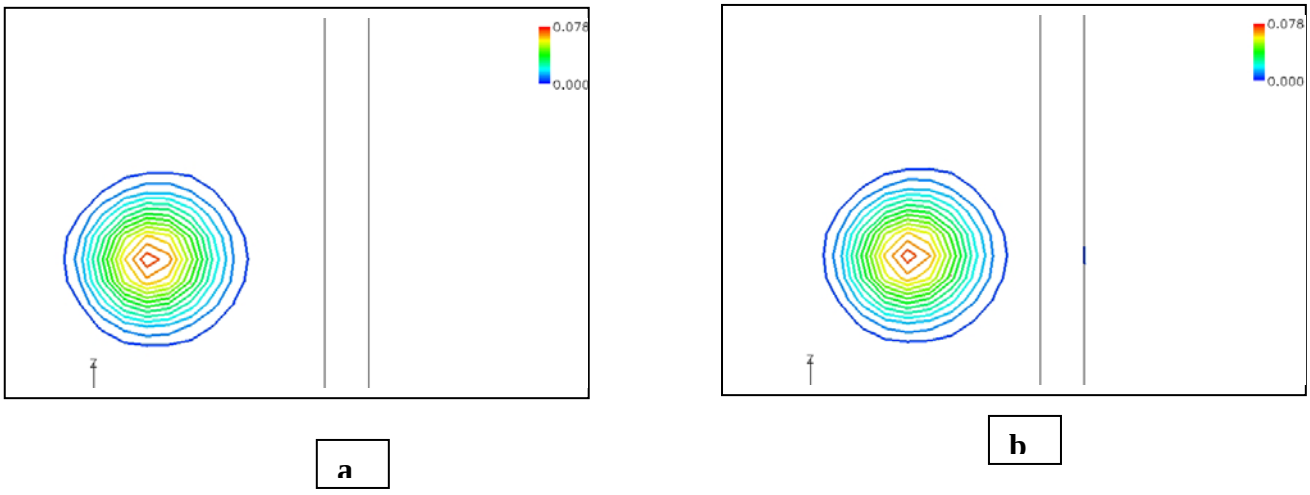

Figure 8. Vorticity contours showing Lamb's vortex propagation across interface. Method-2: Uniformly 7th order ENO computation over the entire domain, using one-sided stencils near boundaries.

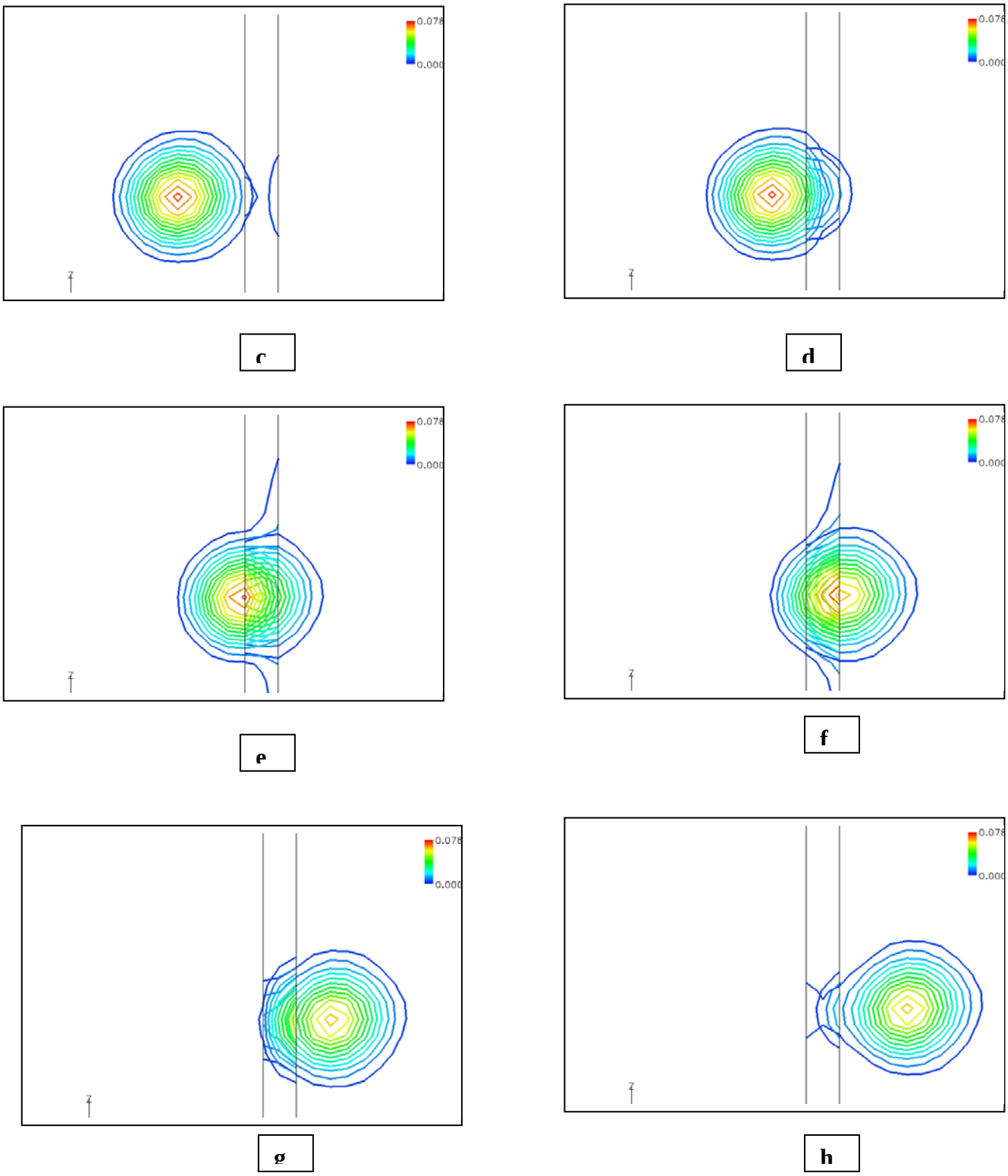

Figure 8(continued). Vorticity contours showing Lamb's vortex propagation across interface. Method-2: Uniformly 7th order ENO computation over the entire domain, using one-sided stencils near boundaries.

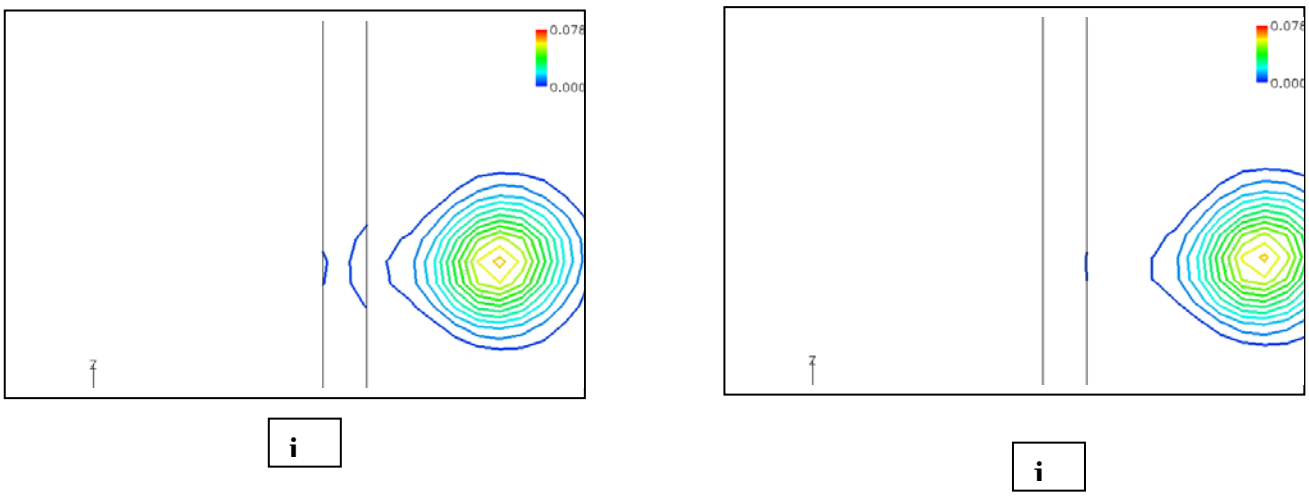

Figure 8(continued). Vorticity contours showing Lamb's vortex propagation across interface. Method-2: Uniformly 7th order ENO computation over the entire domain, using one-sided stencils near boundaries.

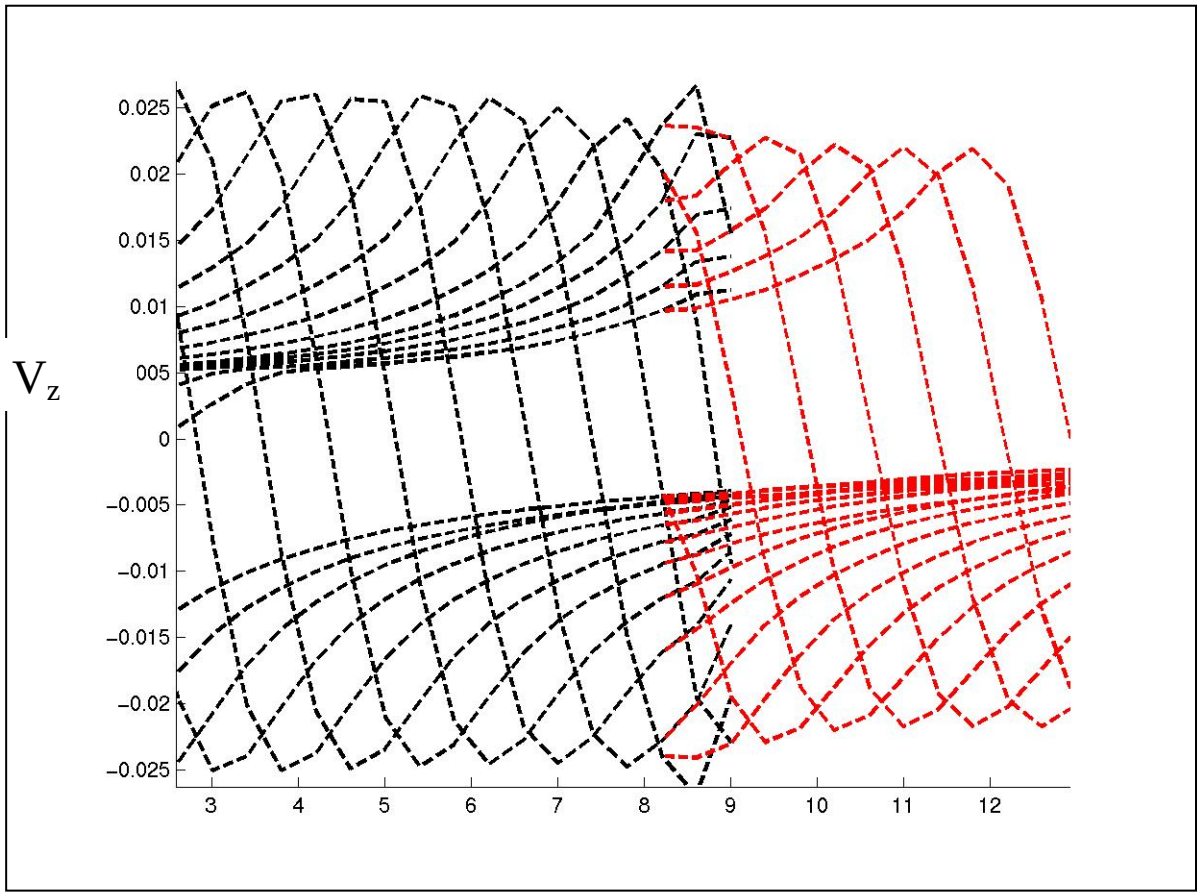

Figure 9. Tangential velocity across the vortex, as it convects through the interface (Black is on Grid-1, Red is on Grid-2). Method-2: Uniformly 7th order ENO computation over the entire domain, using one-sided stencils near boundaries.

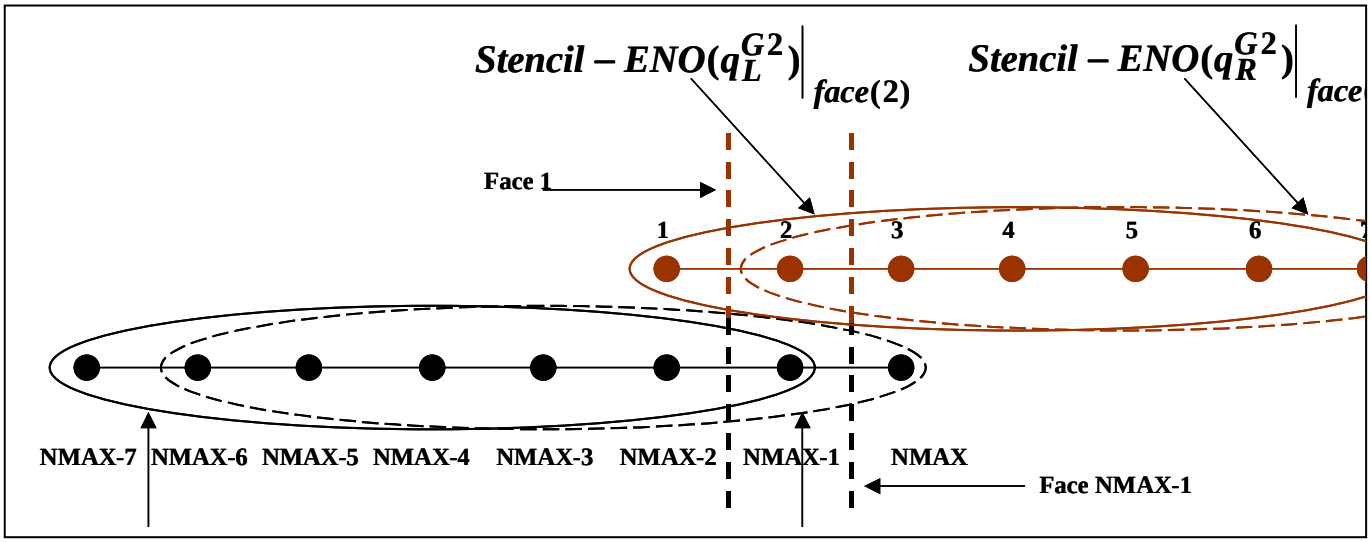

Figure 10. Schematic of the treatment of the fluxes near the overset interface. Method-3: Uniformly 7^{th} order ENO computation over the entire domain, using one-sided stencils near boundaries, and flux projection on overset cell faces.

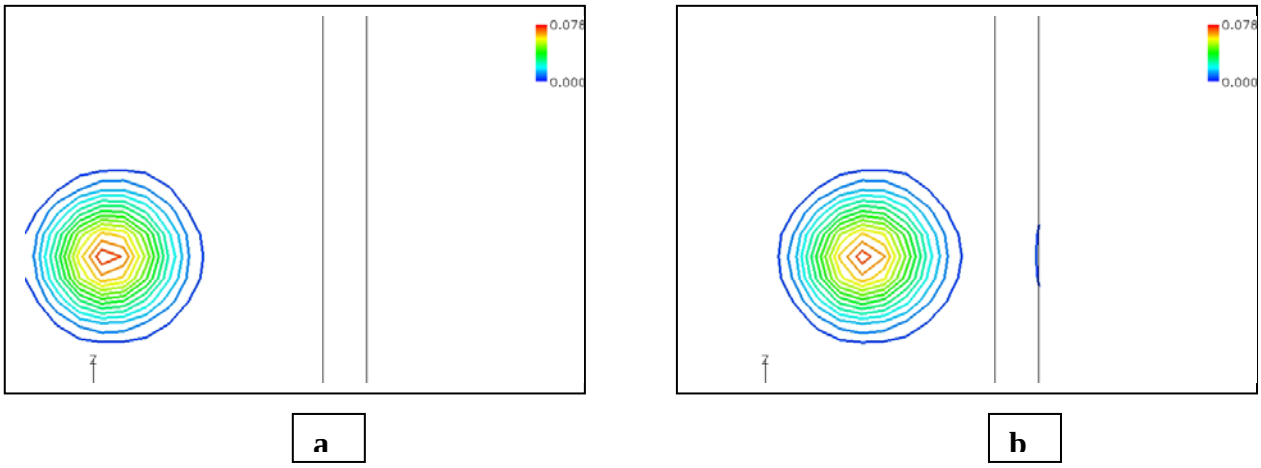

Figure 11. Vorticity contours showing Lamb's vortex propagation across interface. Method-3: Uniformly 7^{th} order ENO computation over the entire domain, using one-sided stencils near boundaries, and flux projection on overset cell faces.

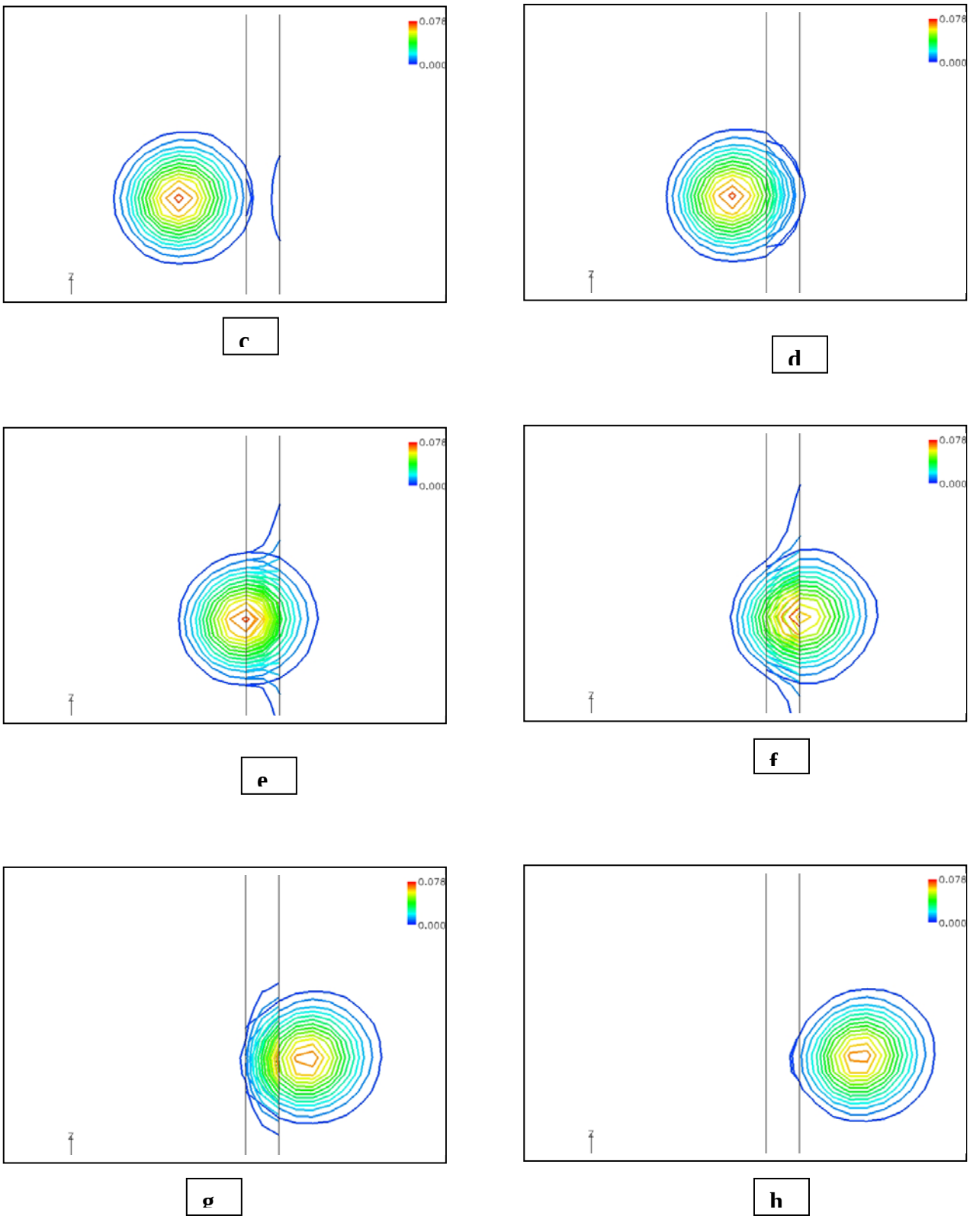

Figure 11(continued). Vorticity contours showing Lamb's vortex propagation across interface. Method-3: Uniformly 7th order ENO computation over the entire domain, using one-sided stencils near boundaries, and flux projection on overset cell faces.

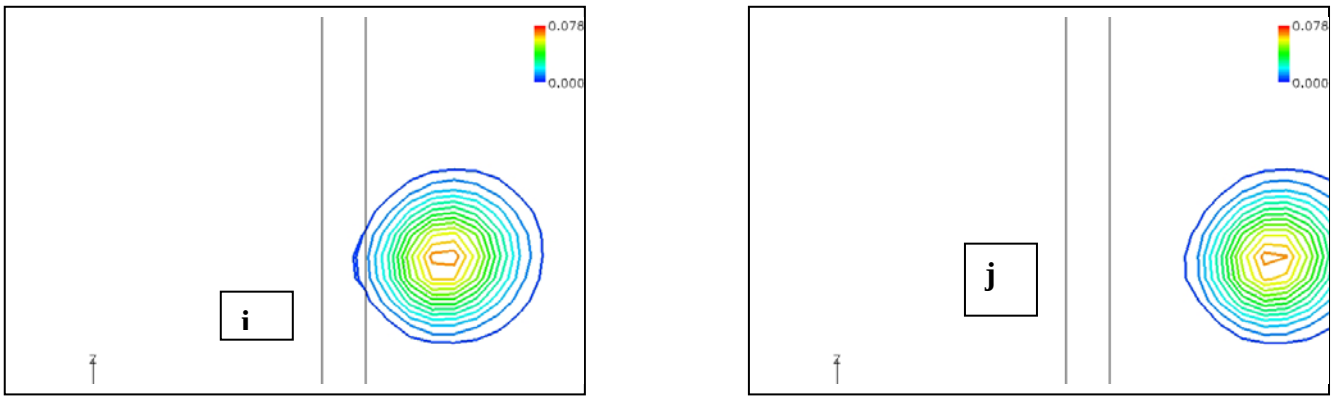

Figure 11(continued). Vorticity contours showing Lamb's vortex propagation across interface. Method-3: Uniformly 7th order ENO computation over the entire domain, using one-sided stencils near boundaries, and flux projection on overset cell faces.

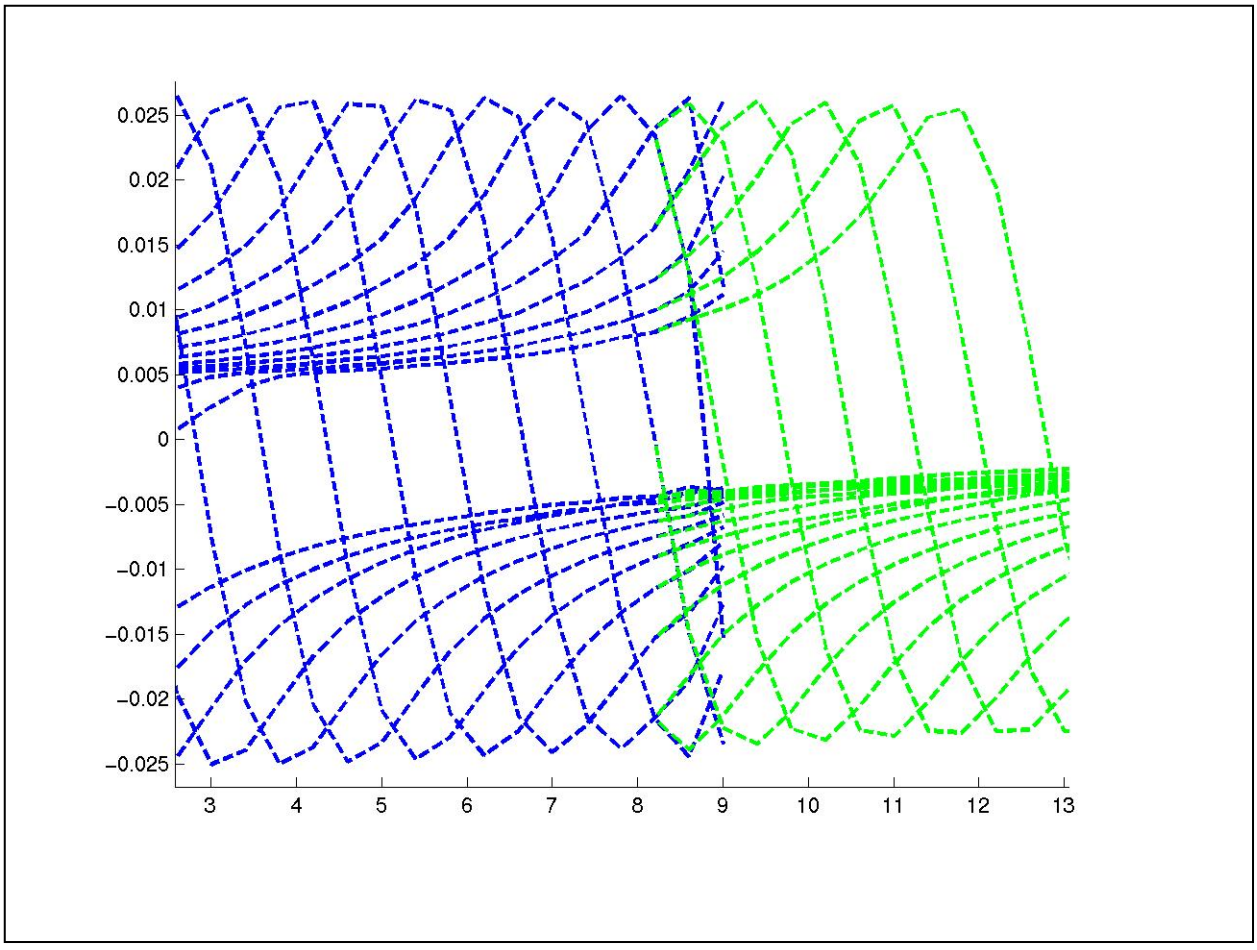

Figure 12. Tangential velocity across the vortex, as it convects through the interface (Blue is on Grid-1, Green is on Grid-2). Method-3: Uniformly 7th order ENO computation over the entire domain, using one-sided stencils near boundaries, and Chimera flux interpolation

V_z

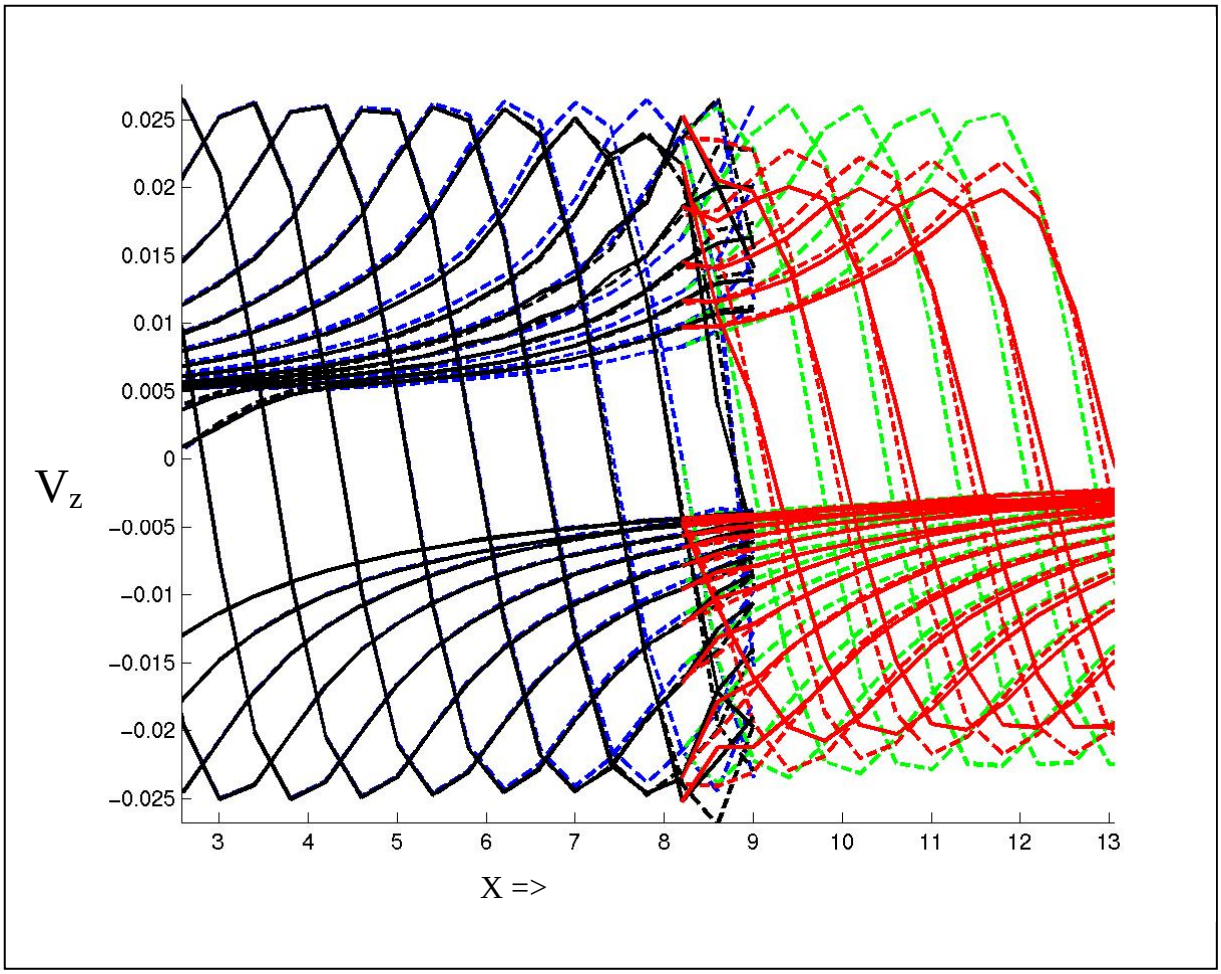

Figure 13. Tangential velocity across the vortex, as it convects through the interface. Comparison of results from Method-1, 2, and 3.

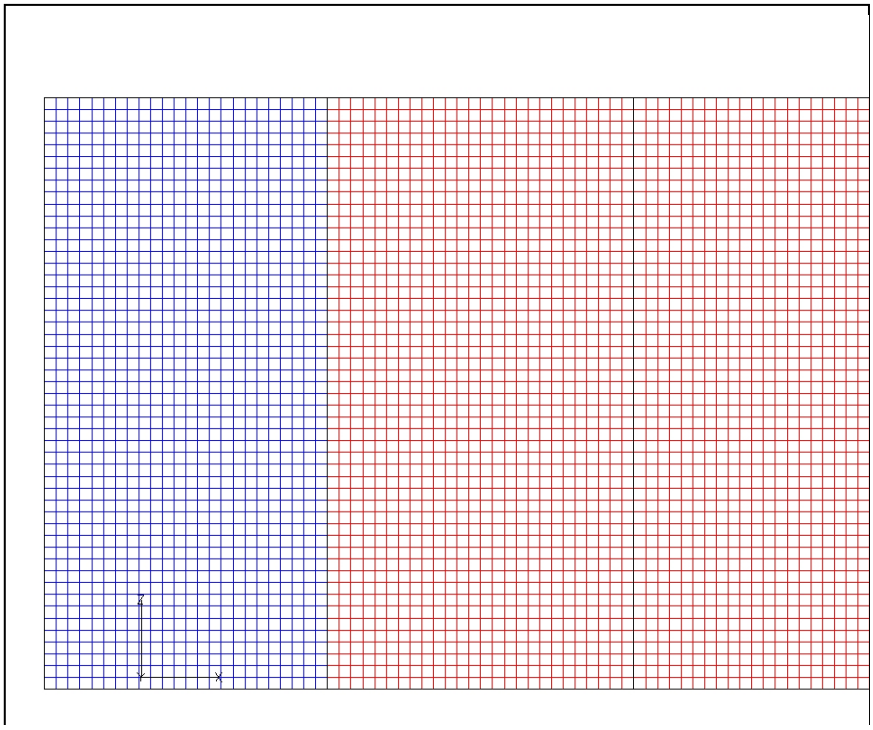

Figure 14. Grid system for overset transfer with excess overlap.

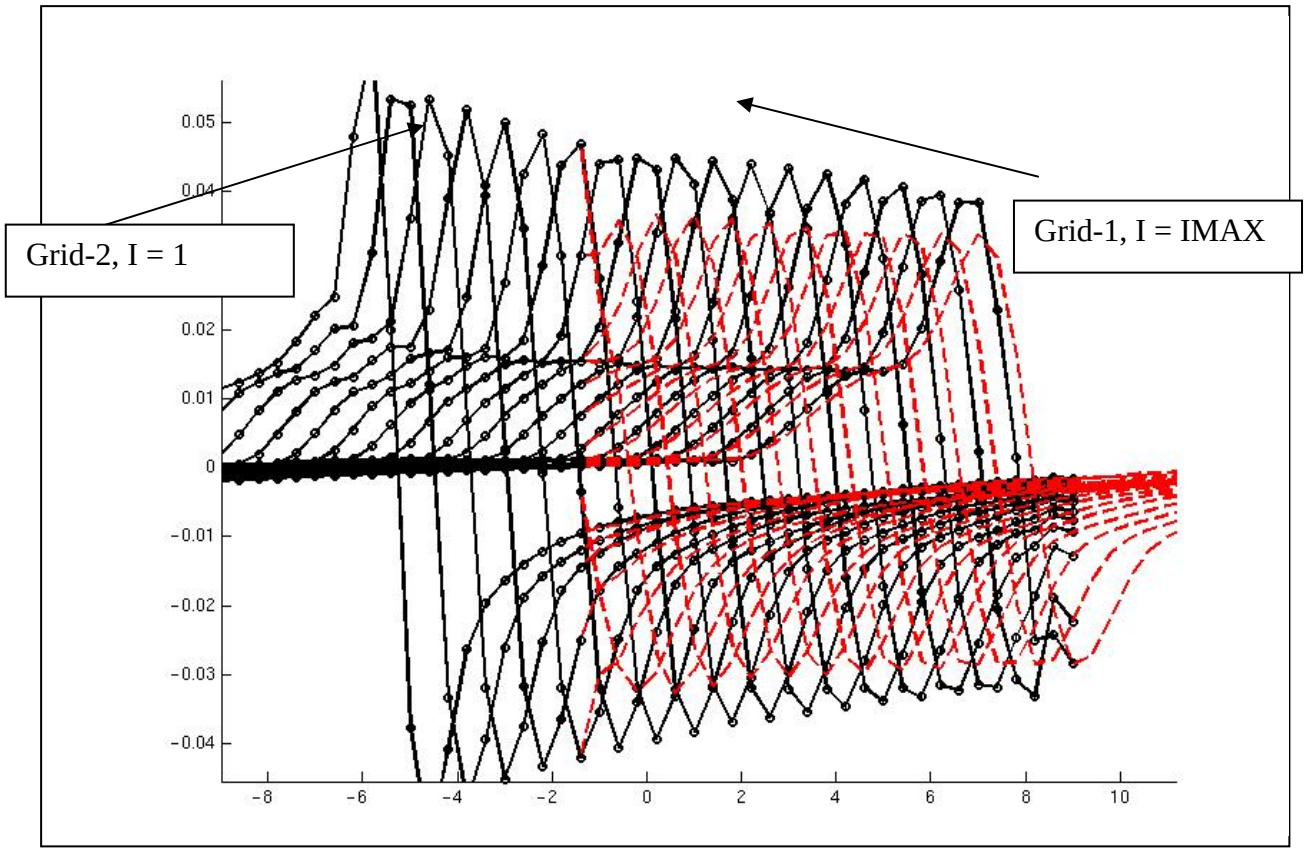

Figure 15. Tangential velocity across the vortex, as it convects through the extended interface (Black is on Grid-1, Red is on Grid-2). Method-1: Uniformly 7th order ENO computation, first order near the boundaries. 4 points across initial core.

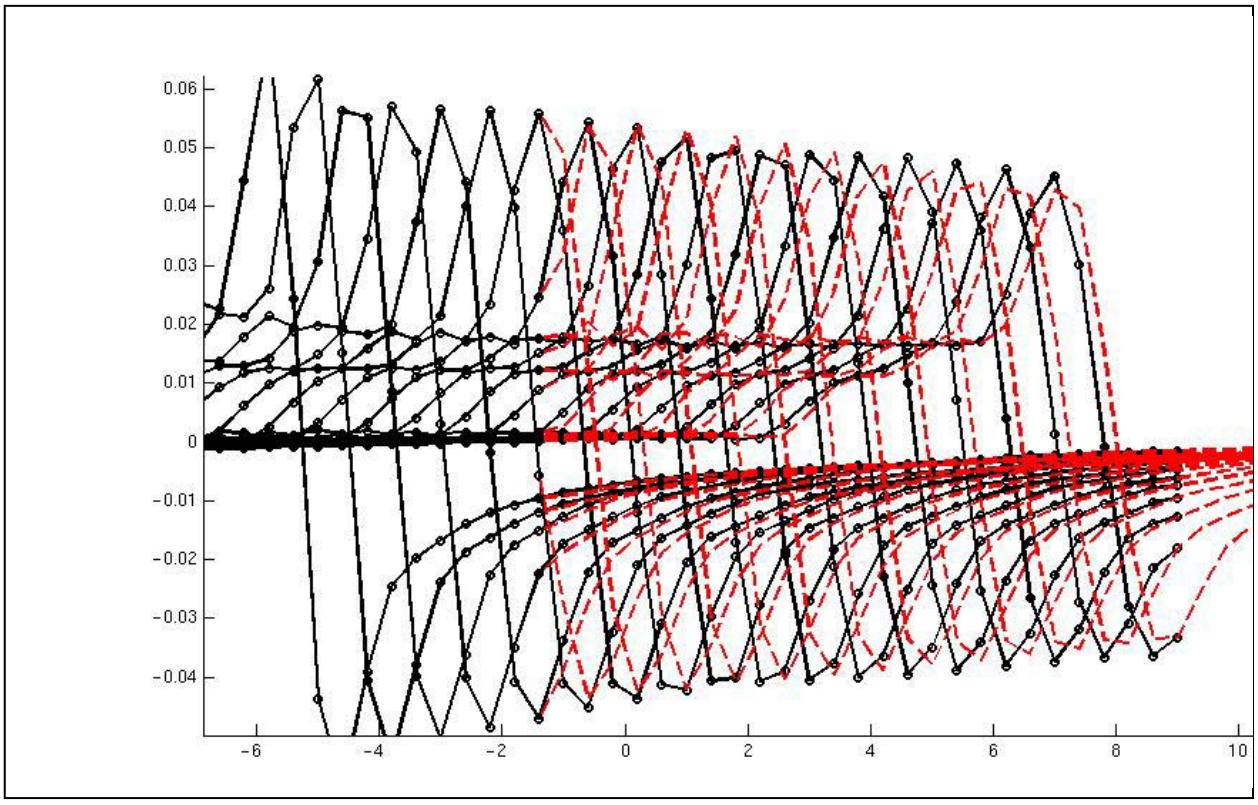

Figure 16. Tangential velocity across the vortex, as it convects through the extended interface (Black is on Grid-1, Red is on Grid-2). Method-2: Uniformly 7th order ENO computation over the entire domain, one-sided stencils near the boundaries. Four points across initial core.

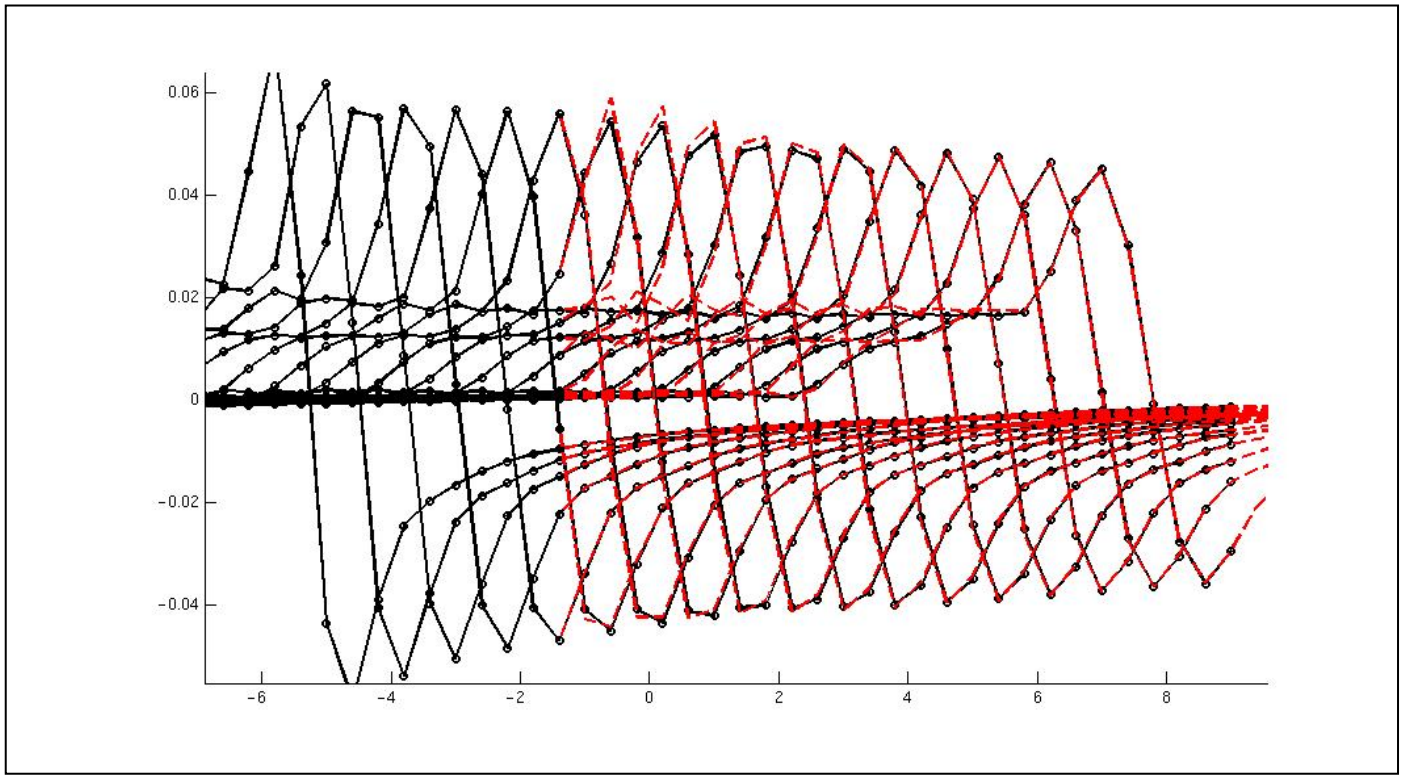

Figure 17. Tangential velocity across the vortex, as it convects through the extended interface (Black is on Grid-1, Red is on Grid-2). Method-3: Uniformly 7th order ENO computation over the entire domain, using one-sided stencils near boundaries, and Chimera flux interpolation. Four points across initial core.

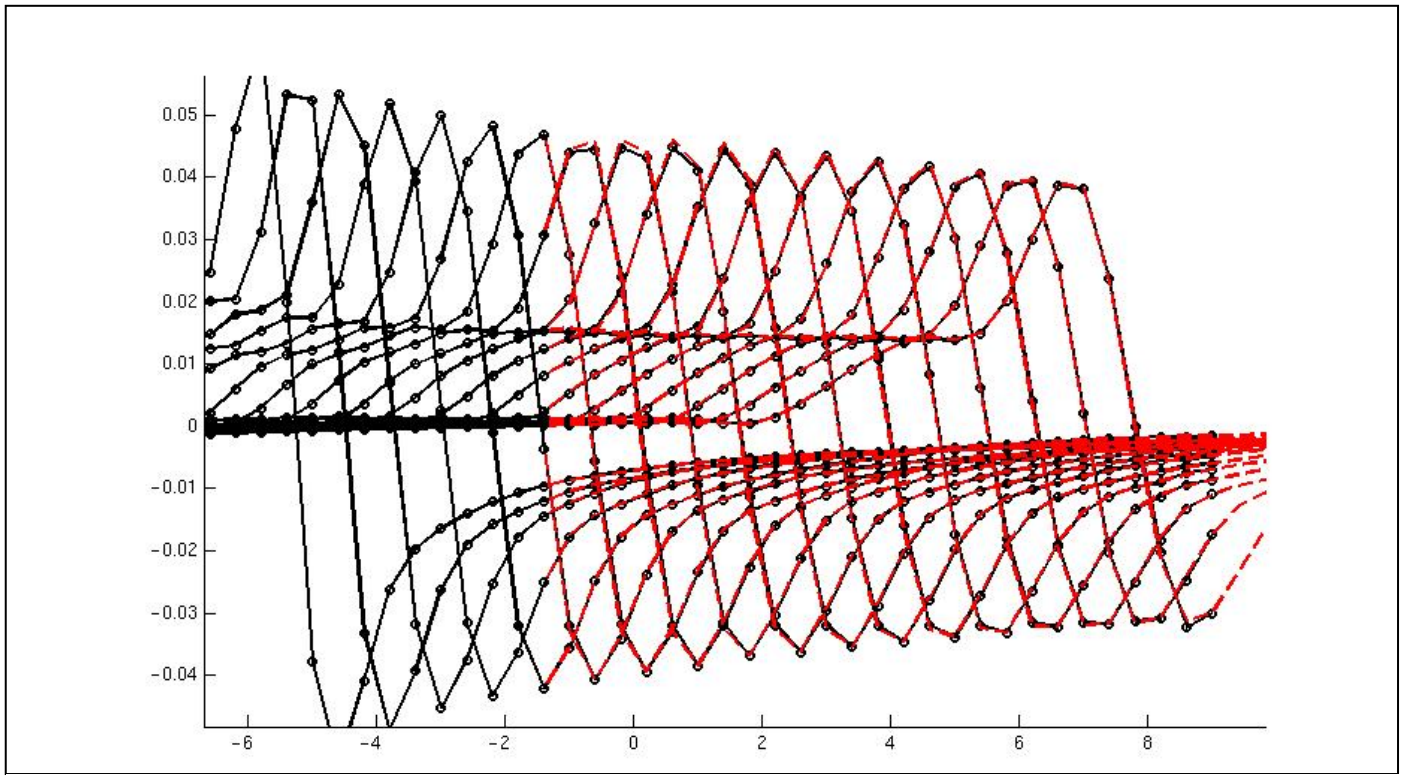

Figure 18. Tangential velocity across the vortex, as it convects through the extended interface (Black is on Grid-1, Red is on Grid-2). Method-3: Uniformly 5th order ENO computation over the entire domain, using one-sided stencils near boundaries, and Chimera flux interpolation. Four points across initial core.

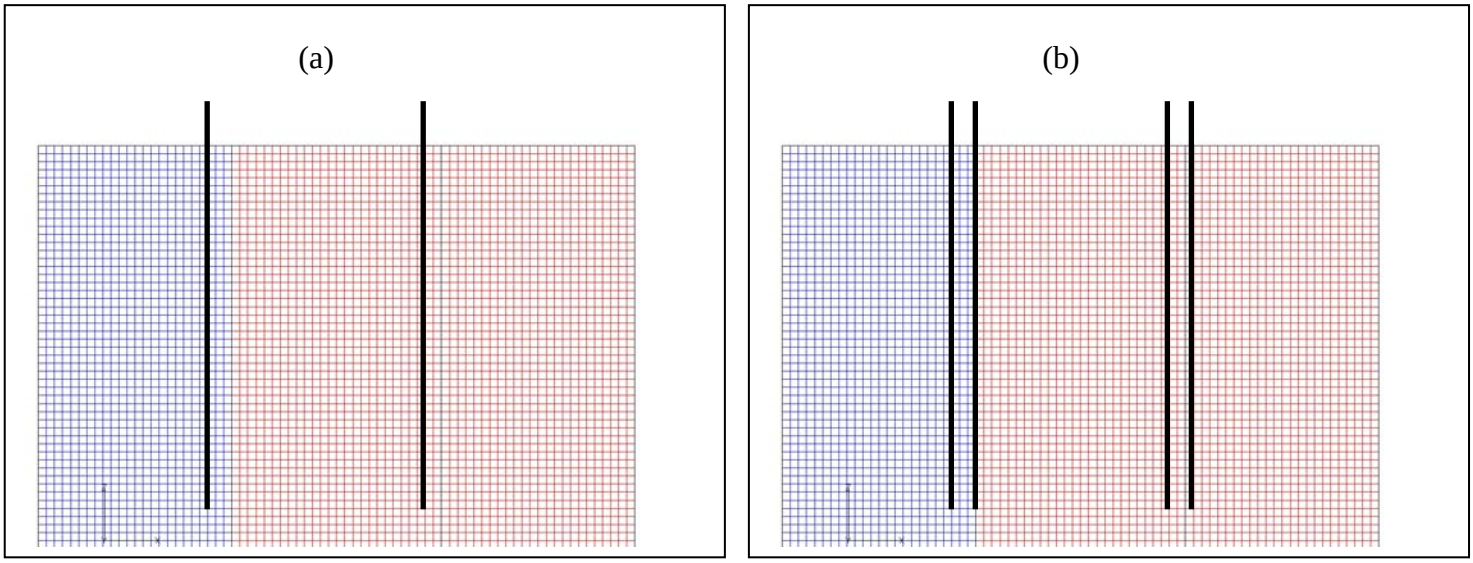

Figure 19. (a) Single, and (b) Double layer of overset interpolation

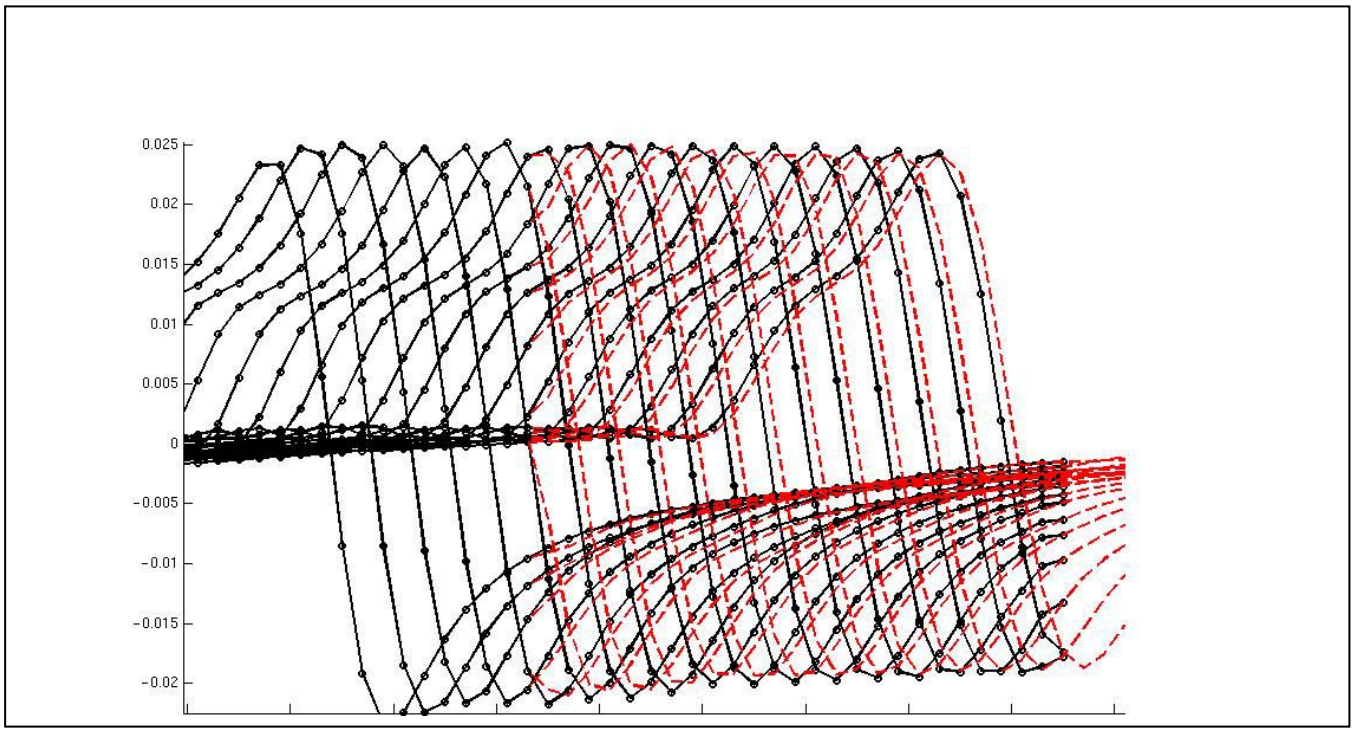

Figure 20. Tangential velocity across the vortex, as it convects through the extended interface (Black is on Grid-1, Red is on Grid-2). Method-2: 7^{th} order ENO computation over the entire domain, using one-sided stencils near boundaries, and single-layer interpolation. Six grid points across initial vortex core.

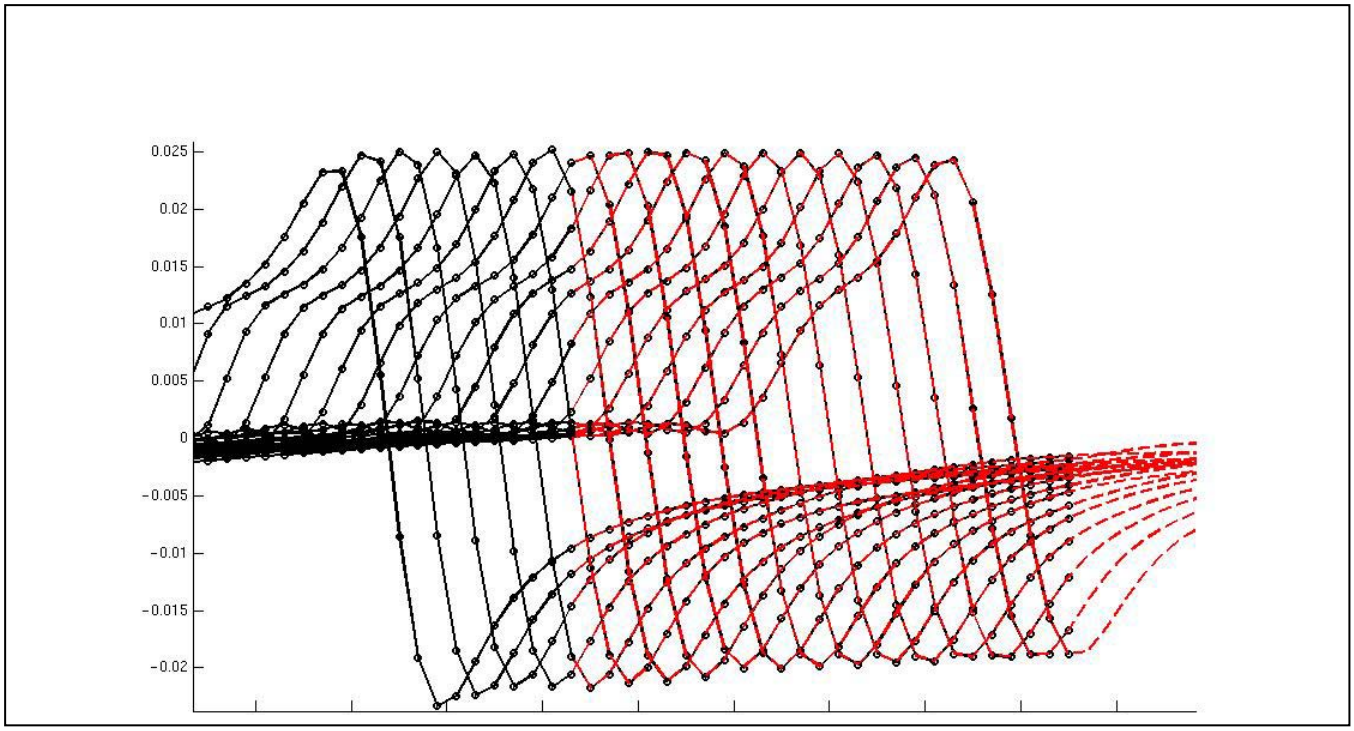

Figure 21. Tangential velocity across the vortex, as it convects through the extended interface (Black is on Grid-1, Red is on Grid-2). Method-2: 7^{th} order ENO computation over the entire domain, using one-sided stencils near boundaries, and double-layer interpolation. Six points across initial vortex core.

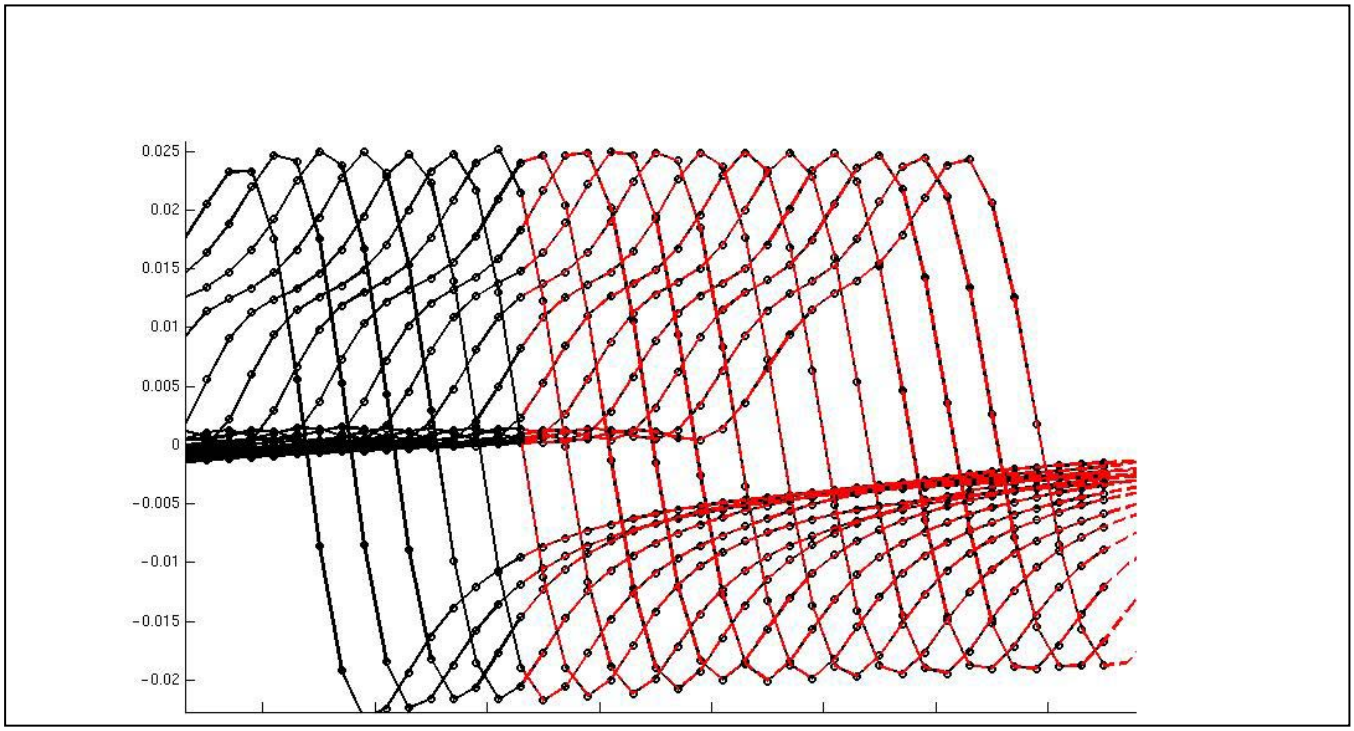

Figure 22. Tangential velocity across the vortex, as it convects through the extended interface (Black is on Grid-1, Red is on Grid-2). Method-2: 7^{th} order ENO computation over the entire domain, using one-sided stencils near boundaries, and triple-layer interpolation. Six points across initial vortex core.

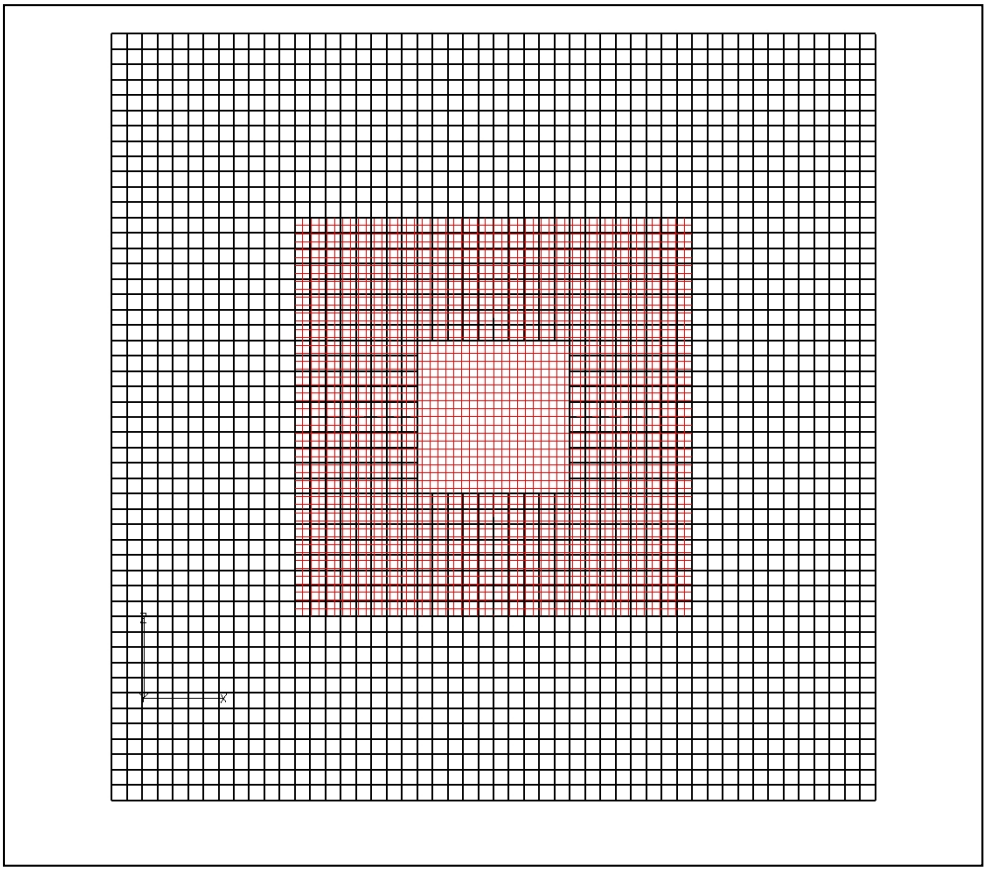

Figure 23. Overset grids with 2:1 grid resolution. Finer grid is entirely inside the coarse grid. Vortex is transferred to the coarser grids through internal boundary points ("fringe points").

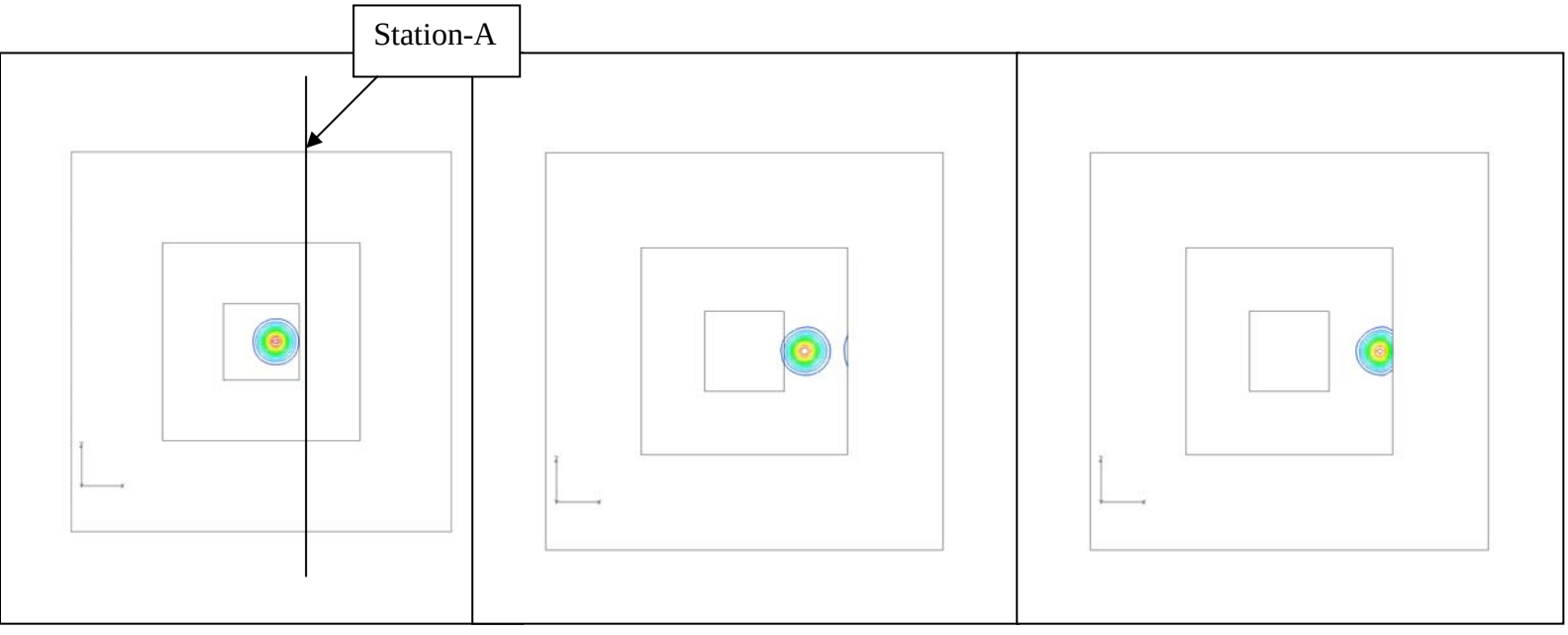

Figure 24a. Vorticity contours plotted on Grid-1. Method-2: 7^{th} order ENO computation over the entire domain, using one-sided stencils near boundaries, and single-layer interpolation

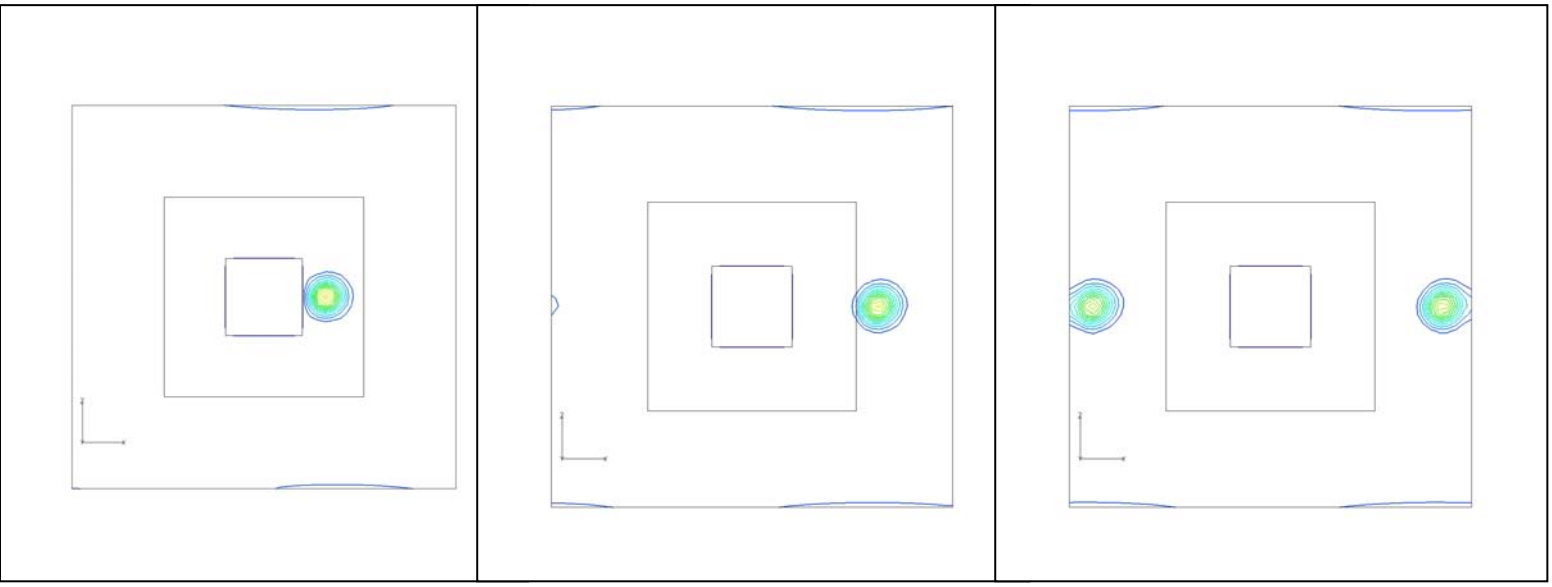

Figure 24b. Vorticity contours plotted on Grid-2. Method-2: 7th order ENO computation over the entire domain, using one-sided stencils near boundaries, and single-layer interpolation.

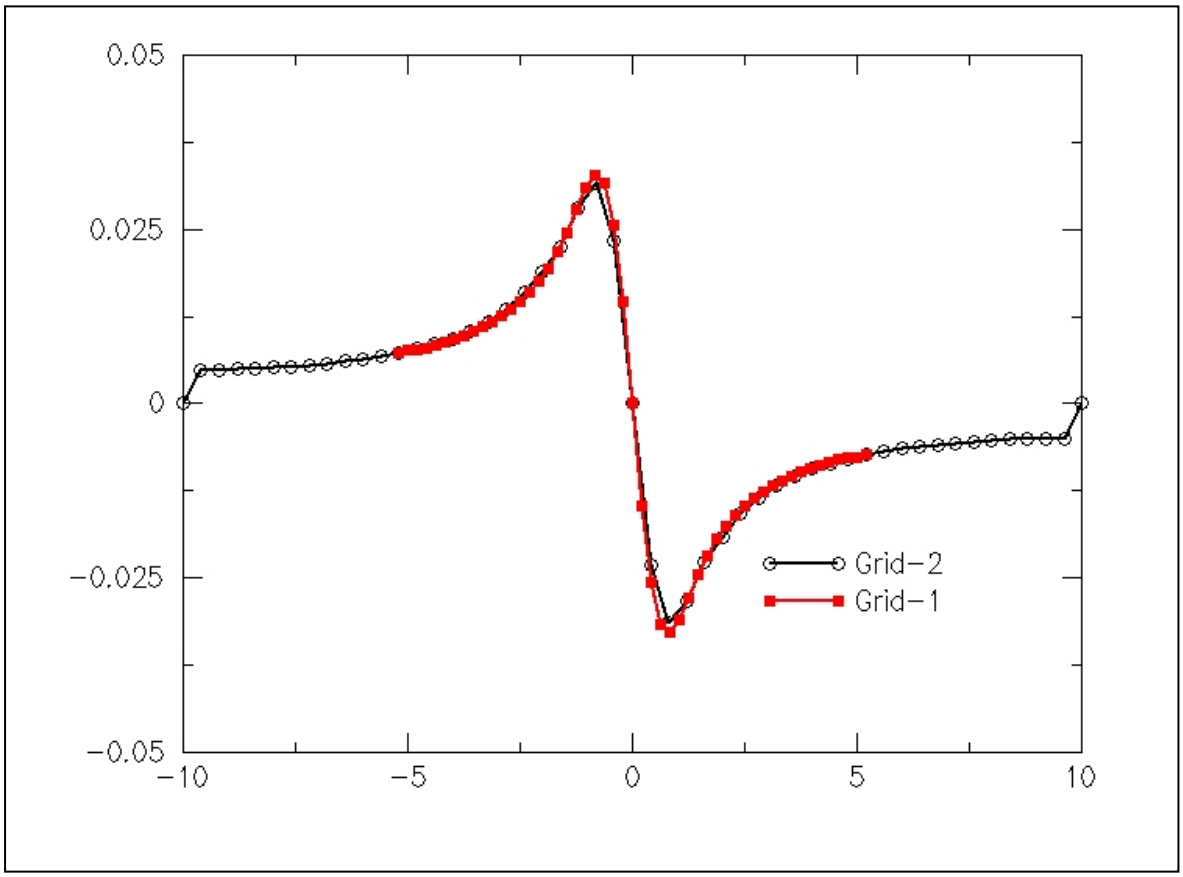

Figure 25. Tangential velocity across the vortex, at station-A (shown in figure 24a). Method-2: 7th order ENO computation over the entire domain, using one-sided stencils near boundaries, and single-layer interpolation. Nine grid points across the vortex core in Grid-1, and five grid points in Grid-2.

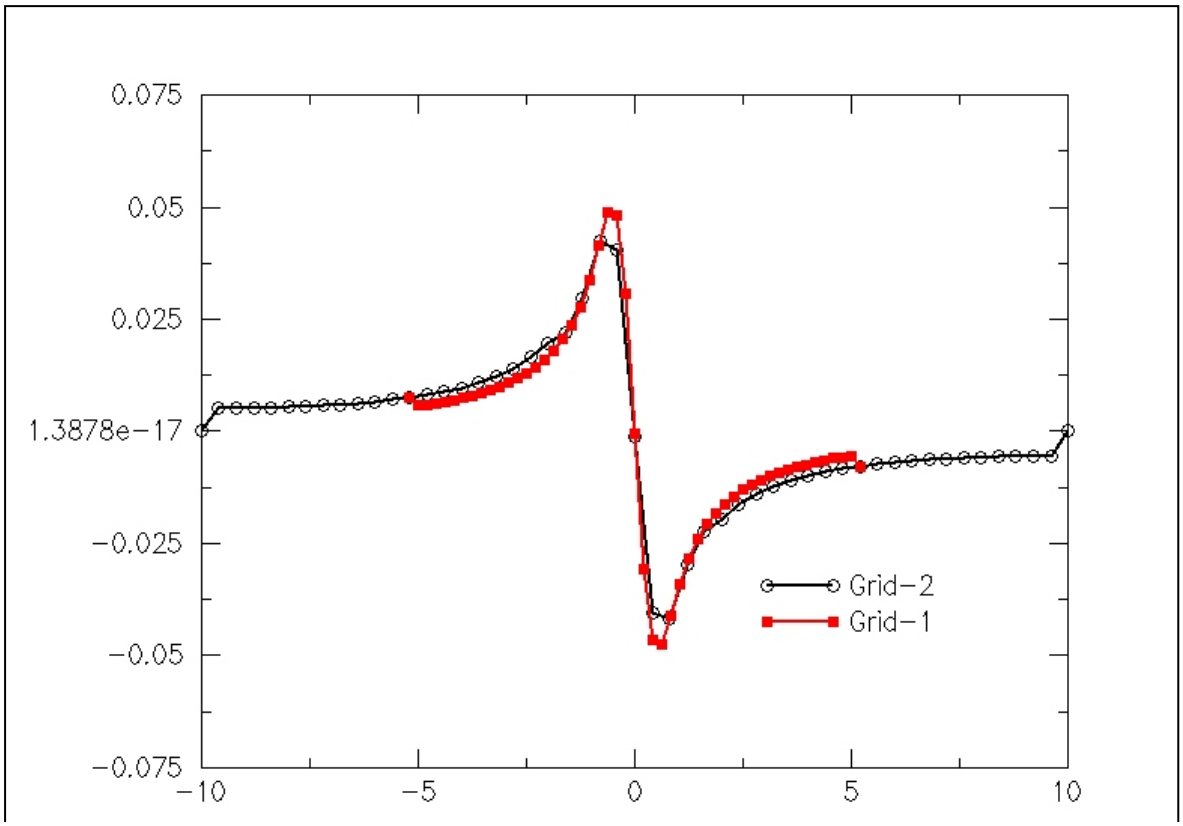

Figure 26. Tangential velocity across the vortex, at station-A(shown in figure 24a). Method-2: 7th order ENO computation over the entire domain, using one-sided stencils near boundaries. Seven grid points across the vortex core in Grid-1, and four grid points in Grid-2.

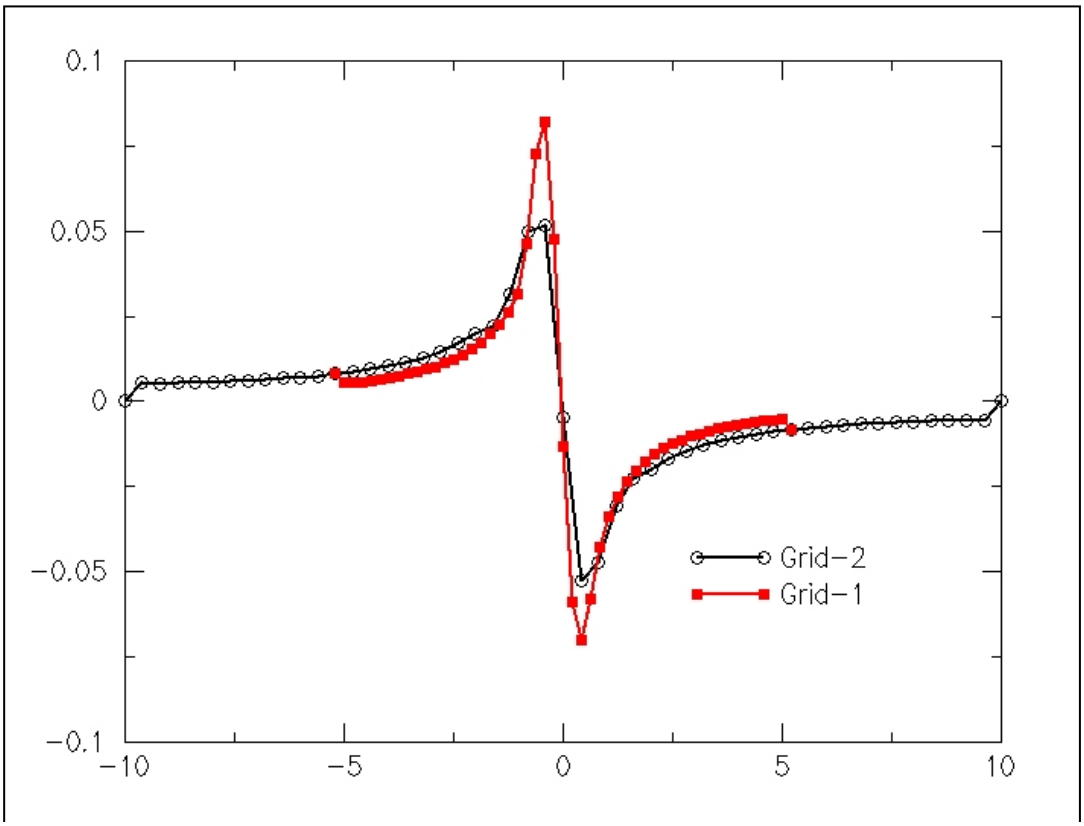

Figure 27. Tangential velocity across the vortex, at station-A (shown in figure 24a): 7th order ENO computation over the entire domain, using one-sided stencils near boundaries, and single-layer interpolation. Five grid points across the vortex core in Grid-1, and three grid points in Grid-2.